Check for updates

Seismic characterisation of multiple BSRs in the Eastern Black Sea Basin

Vanessa Monteleone [a,b,*], Tim A. Minshull [a], Héctor Marín-Moreno [a,c]

[a] *School of Ocean and Earth Science, University of Southampton, National Oceanography Centre, Waterfront Campus, European Way, Southampton, SO14 3ZH, UK*
[b] *National Oceanography Centre, Waterfront Campus, European Way, Southampton, SO14 3ZH, UK*
[c] *Norwegian Geotechnical Institute, Sandakerveien 140, 0484, Oslo, Norway*

A B S T R A C T

Long offset seismic reflection data reveal the presence of four Bottom Simulating Reflectors (BSR0-3) within folded sediments of the Tuapse Trough, along the NE margin of the Eastern Black Sea Basin (EBSB). Multiple BSRs are observed in other sites worldwide, however, their origin and formation mechanisms are still debated. Here, we investigate the formation mechanisms of the EBSB multiple BSRs based on their seismic character and on their physical properties derived from reflected and refracted arrival seismic velocities. Seismic reflection data are downward continued to enhance refracted arrivals. A 2D travel-time velocity model of the subseabed, using combined travel-times from non-downward-continued reflected and downward-continued refracted signals, shows variations in the physical properties at the BSRs and nearby sediments. The P-wave velocity (V_P) increase of 1.55–1.72 km/s between the seafloor and BSR0 (258 mbsf) reflects normal compaction trends in sediments, whereas the V_P of 1.75–1.83 km/s between BSR0 and BSR1 (360 mbsf) is higher than that expected for sediments at that depth. Beneath BSR0, a V_P decrease from 1.83 km/s to 1.61 km/s occurs within a 70-80 m-thick layer including BSR2 (395 mbsf) and extending to BSR3 (438 mbsf). Beneath BSR3, V_P increases. Based on an analytical model linking seismic velocity to physical properties, these V_P trends can be explained by a gas hydrate saturation from 0 to 2% between the seafloor and BSR0, reaching $4 \pm 2\%$ just above BSR1. A free gas saturation of up to 20–25% is estimated within the low-velocity zone between BSR1 and BSR3. BSR1 likely represents the present-day base of the gas hydrate stability zone (BGHSZ), which aligns with the theoretical BGHSZ assuming a geothermal gradient of 26–30 °C/km. Based on seismic polarities and results from travel-time analysis and rock physics modelling, we suggest that hydrate dissociation and recycling processes may explain the negative polarity of BSR2 and BSR3, which are still visible due to the presence of relict gas, and inferred higher gas hydrate saturations close to the present-day base of the stability zone at BSR1. Also, structural and stratigraphic controls seem to have favoured focused free gas flow and hydrate formation at the top of an anticlinal structure, thus likely controlling multiple BSR generation in the EBSB.

1. Introduction

The presence of a Bottom-Simulating Reflector (BSR) in seismic reflection data is commonly interpreted as an indicator for the presence of gas hydrates in marine sediments (e.g., Shipley et al., 1979). The BSR is a distinct reflector generally characterised by a negative impedance contrast resulting from the contrast between high-velocity gas hydrate-bearing sediments above, and low-velocity gas-bearing sediments directly underneath (Singh et al., 1993; Holbrook et al., 1996). As BSRs generally follow the BGHSZ, they are consequently sub-parallel to the seafloor, frequently crosscutting reflectors, and stratigraphic sequences (Shipley et al., 1979). However, the relationship between BSRs and the presence of gas hydrate is not always clear, as changes in lithology, over-compaction of the sediments (e.g., Cook and Tost, 2014), or chemical changes during diagenesis (e.g., Berndt et al., 2004) may also result in a BSR-like reflection.

Multiple BSR-like reflections, subparallel to the seafloor but at different sub-bottom depths, have been observed along both active and passive margins such as the Tumbes basin, offshore Peru (Auguy et al., 2017), the Hydrate Ridge offshore Oregon, USA (Bangs et al., 2005), the continental slope of the Nankai Trough, offshore Japan (Foucher et al., 2002), the North Atlantic margins (Posewang and Mienert, 1999), the Four-Way-Closure Ridge, offshore SW Taiwan (Kunath et al., 2020), the Storegga Slide area on the Norwegian margin (Posewang and Mienert, 1999; Andreassen et al., 2000), the western Ross Sea, Antarctica (Geletti and Busetti, 2011), New Zealand's northern Hikurangi subduction margin (Han et al., 2021) and the Western Black Sea Basin (WBSB) (Zander et al., 2017). These studies have presented different possible explanations for the origin of multiple BSRs, which are considered to represent either (i) remnants of an older BSR that no longer marks the hydrate stability limit, which is in a transient state following pressure and/or temperature changes that perturb the hydrate phase boundary (e.g., Foucher et al., 2002; Zander et al., 2017; Popescu et al., 2006; Bialas et al., 2020), (ii) the base of hydrate layers of different gas composition (e.g., Geletti and Busetti, 2011), (iii) the top and base of the free gas zone or of the hydrate-bearing zone (e.g., Tinivella and Giustiniani, 2013; Posewang and Mienert, 1999), (iv) the boundary between overpressure compartments, which are generally observed at greater

depths compared to the typical thickness of the GHSZ (e.g., Tinivella and Giustiniani, 2013), (v) the result of a combination of recent sedimentation, tectonic uplift and/or fluid activities at subduction margins (e.g., Crutchley et al., 2019; Han et al., 2021), or (vi) unrelated to gas and gas hydrate and related to lithological and/or geochemical changes such as opal-A to opal CT transition (e.g., Berndt et al., 2004; Cook and Tost, 2014). When multiple BSRs are linked to past hydrate stability conditions, a physical explanation is needed for the paleo-BGHSZ remaining visible. It could be that gas or gas hydrate is left behind (e.g., Bangs et al., 2005; Popescu et al., 2006), or that the remnants have a different pore structure and solid grains orientation after hydrate dissociation due to pore collapse or, depending on whether gas hydrate is stable or not, there is a geochemical mechanism e.g., the formation of greigite (Kars et al., 2021, and references therein).

Semi-isolation from marine circulation, cyclic periods of anoxia, and high sedimentation rates depositing large amounts of terrestrially sourced, organic-rich deposits, favour gas hydrate generation in the Black Sea (Vassilev and Dimitrov, 2002; Egorov et al., 2011). Abundant seepage and mud volcanoes are present along the basin's margins, and evidence of fluid accumulation and escape features on regional seismic reflection profiles (i.e., seismic blanking, gas pipes and chimneys, bright spots) are associated with the presence of biogenically sourced gas and hydrates within the shallow stratigraphic units of the Black Sea (e.g., Starostenko et al., 2010; Pape et al., 2011, 2021; Popescu et al., 2007; Egorov et al., 2011). Furthermore, thermogenic gas may be sourced from deeper stratigraphic levels, particularly from the Oligocene-lower Miocene organic-rich Maykop Formation (e.g., Simmons et al., 2018).

Previous studies have focused on seismic BSRs within the Danube and Dnieper delta and deep-water fans of the WBSB (Fig. 1). Here, multiple BSRs have been identified as mostly discontinuous seismic events limited to few areas (e.g., Popescu et al., 2007; Zander et al., 2017) (Fig. 1). These features are predominantly interpreted to result from the combined effect of increased sedimentation rates along the basin's margins and/or climatic change (i.e., sea-level and/or temperature variations) following the Last Glacial Maximum (LGM, e.g., Popescu et al., 2006; Zander et al., 2017).

In the Eastern Black Sea Basin (EBSB), studies have identified the presence of single seismic BSRs along the offshore margins of Crimea, Georgia, and Turkey (Fig. 1). The only mention to the presence of possible multiple BSRs come from a prospect by Rosneft Company and Moscow State University researchers on gas hydrates in the Tuapse Trough (Shnyukov, 2013). According to Shnyukov (2013), oil-bearing cores were recovered at several sites in the Tuapse Trough and along their sections "three repetitive BSR boundaries of controversial nature" have been identified. However, no other information is available on these BSRs.

This study aims to investigate the nature of four BSRs observed, for the first time to our knowledge, within the upper Miocene-Quaternary sedimentary section of the Tuapse Trough, on the NE margin of the EBSB (Fig. 1). Previous work has focused on explaining the cause(s) of the shift in the BGHSZ and corresponding BSR, rather than on understanding the physical parameters making the paleo-BGHSZ still reflective. However, there are different implications for polarity/velocity contrasts depending on the mechanism responsible for the presence of
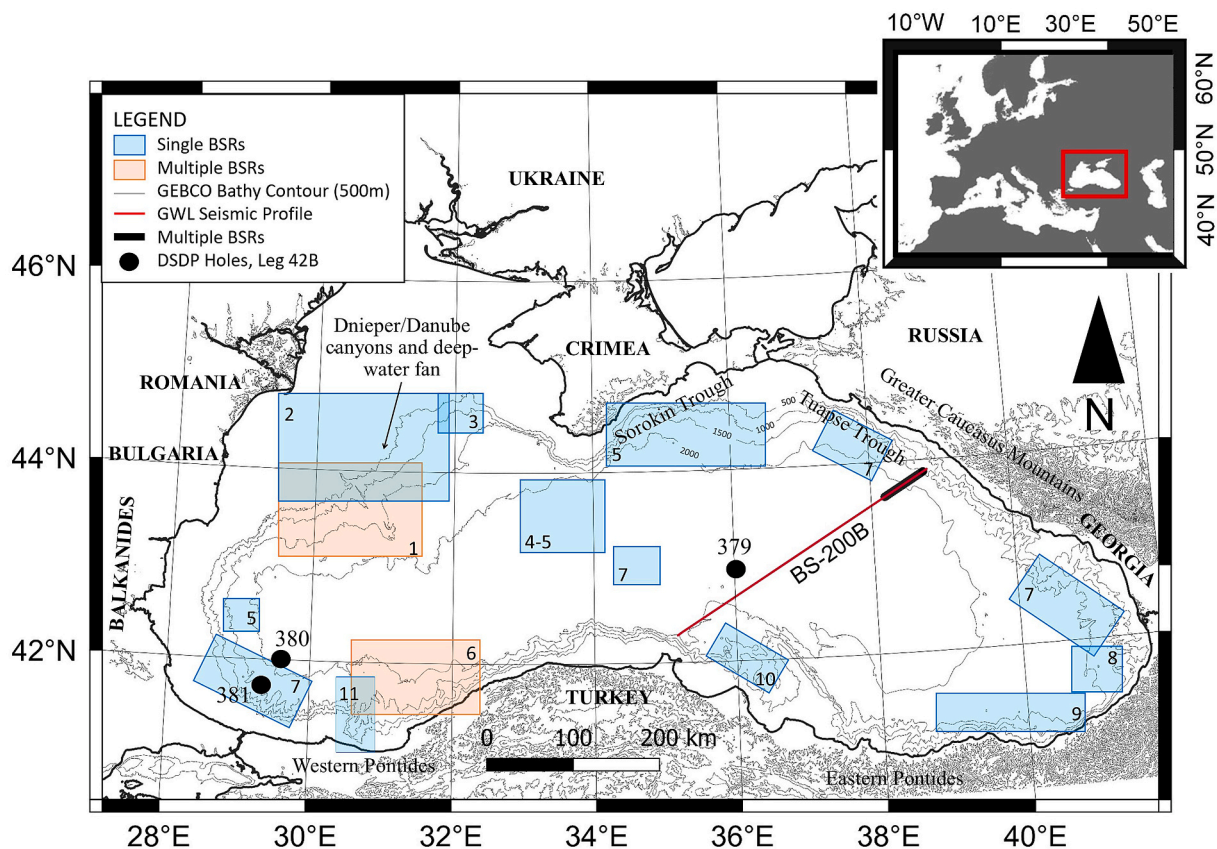

Fig. 1. Topography and bathymetry of the Black Sea region contoured at a 500 m interval (GEBCO Compilation Group, 2019, https://www.gebco.net/). A single seismic profile (BS–200B; red line), belonging to a regional seismic survey from GWL, is used in this study (Figs. 2 and 3). The thick black segment to the NE-end of the profile shows the location of the multiple BSRs identified in this study. Numbered black circles show the DSDP Holes 379, 380 and 381 locations (Ross, 1978). Boxes overlaid on map represent the locations of studies previously identifying single BSRs (blue boxes) and multiple BSRs (orange boxes) across the whole Black Sea region ([1]Zander et al., 2017, Bialas et al., 2020, Popescu et al., 2006, Gassner et al., 2019; [2]Riedel et al., 2020, Ker et al., 2019, Hillman et al., 2018; [3]Zillmer et al., 2005, Lüdmann et al., 2004; [4]Xing and Spiess, 2015; [5]Merey and Sinayuc, 2016; [6]Dondurur et al., 2013, Menlikli et al., 2009; [7]Vassilev and Dimitrov, 2002; [8]Minshull and Keddie, 2010; [9]Cifci et al., 2012; [10]Dondurur and Çifçi, 2009; [11]Nasif et al., 2020).

multiple BSRs on seismic data. Here, we look more closely at the physical properties associated with the seismic evidence of multiple BSRs, aiming to constrain the mechanisms linked with their generation.

We obtain the physical properties of BSR reflectors from the analysis of pre-stack multichannel seismic reflection data. These data are used to define a 2D compressional wave (V_P) velocity model for the shallow sediments using the travel-time forward modelling approach described by Zelt and Smith (1992). The 10.2 km-long offset recording of the seismic reflection profile used in this study, allows refracted arrivals to be imaged at far offsets within shot gathers. We apply downward continuation of these data to a datum closer to seafloor (Berryhill, 1979, 1984; Harding et al., 2007). Our aim was to be able to pick refractions from shallow stratigraphic levels (i.e., BSRs depths) at closer offsets, thus providing valuable travel-time information for velocity modelling. We then compare the BSR depths constrained by travel-time analysis against the expected depth for the present-day BGHSZ, calculated from a compilation of regional data (i.e., seafloor temperature, geothermal gradient, pore water salinity). Finally, we use the velocities from travel-time analysis and a rock physics model to provide an estimate of free gas and gas hydrate saturation.

Results from this study aim to highlight: (i) the link between multiple BSRs and the physical properties of sediments and (ii) the formation mechanisms that can explain the origin of multiple BSRs in the EBSB. Furthermore, our study illustrates some of the advantages and limitations of applying downward continuation to streamer data for shallow targets in the top few hundred meters below seafloor.

2. Geological setting

The Black Sea is a semi-isolated basin located between the Pontide Mountains in Turkey to the south, the Caucasus Mountains to the east, and the relatively low coastal regions of Ukraine and Balkan countries to the west (Fig. 1). The basin is underlain by a flat, 2.0–2.2 km-deep abyssal plane that obscures two separate depocenters, the Western Black Sea Basin (WBSB) and the Eastern Black Sea Basin (EBSB). These two sub-basins formed by rifting in the hinterland of the Pontides magmatic arc as result of the subduction of Neotethyan lithosphere below the southern part of the Eurasian continental margin (e.g., Okay et al., 1994; Robinson and Kerusov, 1997; Nikishin et al., 2003; Stephenson and Schellart, 2010).

Following rifting, the Black Sea underwent rapid basement subsidence accompanied by high sedimentation rates, which resulted in the deposition of thick sequences of mainly Tertiary sediments reaching up to 14 km-thick in the central WBSB and up to 8-9 km-thick in the central EBSB (e.g., Okay et al., 1994; Nikishin et al., 2003; Shillington et al., 2008). At present, the margins of the Black Sea are undergoing compressional deformation that has been active since the Eocene (Saintot et al., 2006), or possibly the Palaeocene (Sheremet et al., 2016), and is related to the convergence of the Eurasian and Arabian plates. The Oligocene period is traditionally considered as the beginning of the syn-collisional (orogenic) stage forming the Caucasus Mountain range to the east of the Black Sea basin, causing the uplift of some areas within tectonic units as well as the reactivation of older fault systems and the formation of inverted structures (Figs. 2 and 3). This time also represents the onset of deposition of the Oligocene-lower Miocene organic-rich shale, formally the regional source-rock of the Black Sea basin: the Maykop Formation (Tari and Simmons, 2018). Compressive deformation has predominantly concentrated around the EBSB margins, as shown by seismic reflection data and earthquake locations (Reilinger et al., 2006). This compression has resulted in the folding and thrusting of the upper Miocene to Quaternary infills of the Tuapse and Sorokin troughs, which have thrusted over the shoulders of the Shatsky Ridge, favoured by the presence of the more ductile Maykop units beneath (Fig. 2).

This study focuses on the folded, upper Miocene-Quaternary successions of the Tuapse Trough, a 40 km-wide and 270 km-long, NW-SE-oriented trough representing the foreland basin of the Greater Caucasus thrust belt (e.g., Adamia et al., 2010; Tari et al., 2018) (Fig. 3). Its stratigraphy mainly consists of a thick sequence of Maykop shale, located at the base and squeezed in between the folded and thrusted upper Miocene-Quaternary units. These units have been transported and deposited within the trough during the uplift of the Greater Caucasus (e. g., Meisner et al., 2009; Adamia et al., 2010; Tari et al., 2018; Vincent et al., 2007). The Tuapse Trough formed under marine conditions in lower Eocene to upper Eocene times (e.g., Tugolesov and Gorshkov, 1985). Compressional uplift started at ~10 Ma during the upper Miocene, with the most intensive folding taking place in the last 5 Myr (Pliocene) (Milanovsky, 1991). The more ancient folds are located in the NE part of the Tuapse Trough, in a zone where the Tuapse Trough joins with the southern slope of the Greater Caucasus, while the youngest folds are located to the SW in the western frontal part of the trough, where the Tuapse Trough abuts the Shatsky Ridge (Tugolesov and Gorshkov, 1985). The sedimentary section of the Tuapse Trough is, therefore, dominated by active growth of the fold system, with folds that are usually expressed as anticlines generating relief as submarine ridges up to 400–600 m high (Almendinger et al., 2011) (Fig. 2). Growth of anticlines continues at present, with erosion of the ridges and sedimentation in isolated mini basins (Almendinger et al., 2011).

3. Seismic dataset

This study uses a single, post-stack time-migrated seismic reflection profile acquired as part of a 2D long-offset seismic reflection survey in 2011 by Geology Without Limits (GWL) and ION GXT (Fig. 1). Data were acquired using an 816-channel hydrophone streamer with a maximum offset of 10.2 km, a receiver spacing of 12.5 m, and a towing depth of 9 ± 0.5 m. The source was a 5680 cubic-inch airgun array towed at a depth of 8 ± 0.5 m and the shot interval was 50 m. Profile BS-200B was acquired in a NE to SW direction, with a 200° heading. Further information on acquisition parameters and on the processing sequence applied by GWL is provided by Monteleone et al. (2019) (see their supporting material).

Here, we focus on a 53.1 km-long section of profile BS-200B, extending from the Tuapse Trough (NE) to the central basin (SW) (Figs. 1–3).

3.1. Character and distribution of the multiple BSRs

Up to four, vertically stacked BSRs are visible within the folded sediments of the Tuapse Trough (Figs. 2 and 3). BSRs mimic the seafloor morphology and crosscut dipping reflectors (Fig. 3). The topmost BSR (BSR0) terminates to its SW end on the crest of a folded structure (anticline) and shows a weak seismic amplitude and seafloor-like signal polarity (Fig. 3A and B). Despite showing a weak signal amplitude on the stack profile, BSR0 appears as a clear event on shot gathers, where it is visible at offsets ranging from zero to 3.8 km (channel 1–300; Fig. 4).

Below BSR0, BSR1 is characterised by higher amplitudes and a predominant reversed polarity compared to the seafloor (Fig. 3C). BSR1 appears as a strong reflection on both the stacked profile and within a wide range of offsets (from near offset to ~ 4.5 km) along shot gathers (channel 1–350; Fig. 4). BSR1 crosscuts a dipping seismic reflector showing phase reversal, with a high-amplitude seabed-like polarity above BSR1, and a high-amplitude reversed polarity below BSR1 (Fig. 3D).

A third, weak seismic reflection, BSR2, shows a predominantly reversed polarity (Fig. 3C). However, BSR2's waveforms are more complex than that of BSR1, likely reflecting the complex impedance structure within that layer as well as interference with reflections from sedimentary strata. This aspect makes it difficult to identify clearly the BSR2 reflection event on shot gathers, where it is visible only within a narrow range of offsets (from zero to ~ 1.4 km offset; channel no. 1–110; Fig. 4).
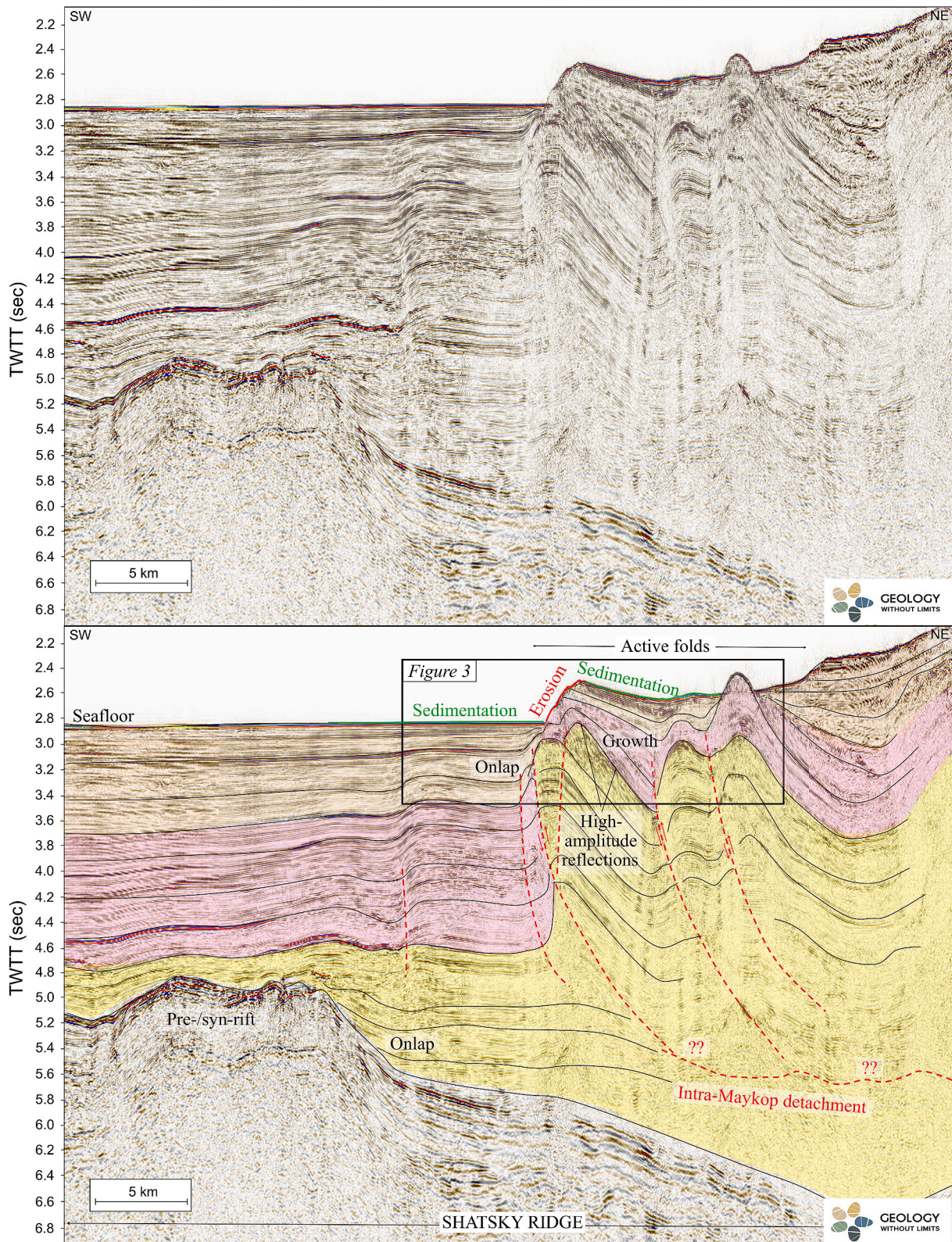
Fig. 2. Non-interpreted (top) and interpreted (bottom) profile BS-200B, showing the thrusted and folded sediments of the Tuapse Trough foreland basin building on top of the Shatsky Ridge. The main structural and stratigraphic features interpreted are the Maykop Formation (yellow), middle-upper Miocene (pink) and Pliocene-Quaternary units (light brown), the main thrust faults and their intra-Maykop basal detachment (red dashed lines), onlaps and growth strata, erosional and depositional domains at the seafloor topography.
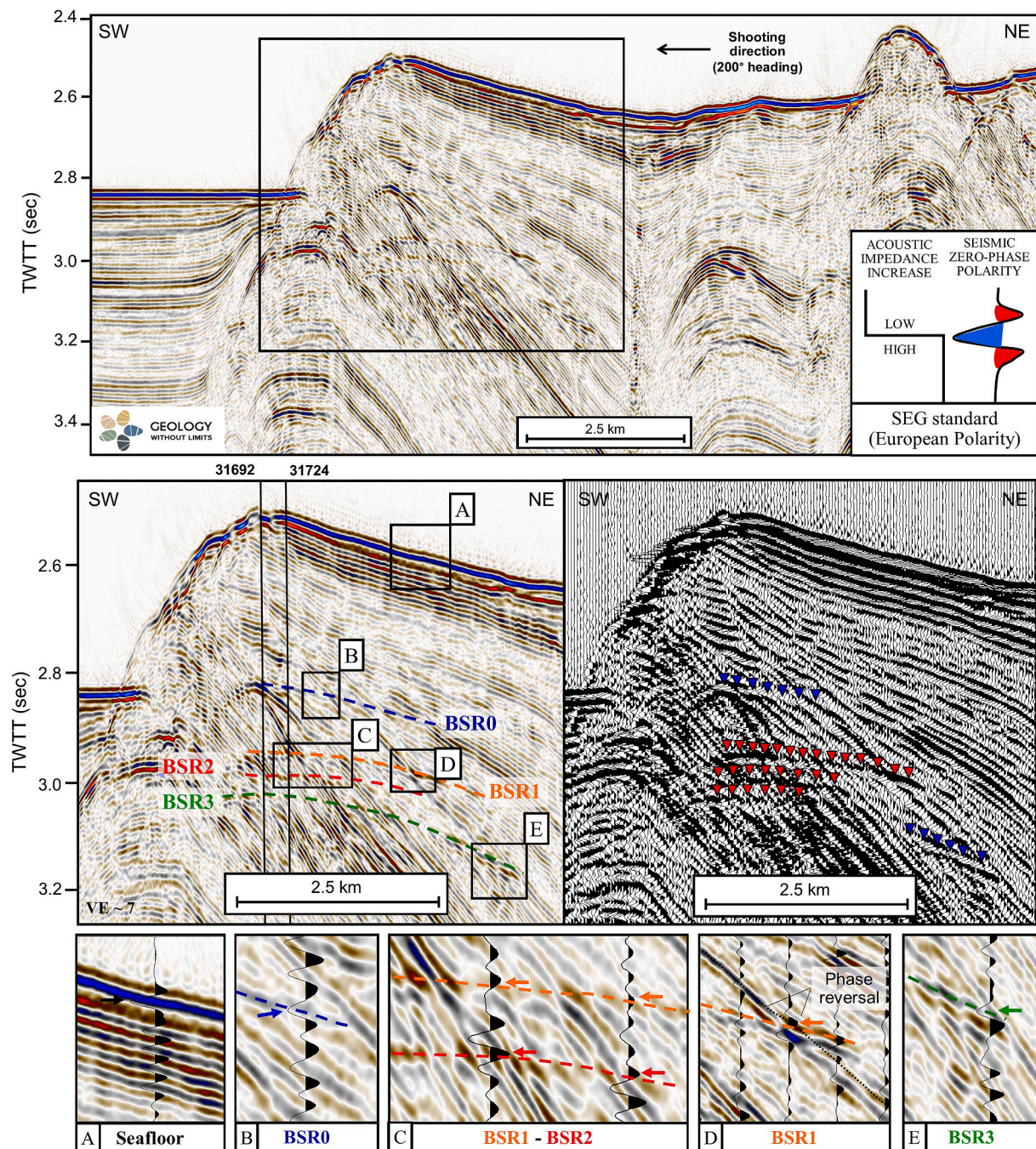
Fig. 3. Seismic reflection profile BS-200B, crossing the upper Miocene-Quaternary folded sediments of the Tuapse Trough. Non-interpreted profile (top) and zoomed, interpreted profile (middle) showing up to four seismic reflections sub-parallel to seafloor and cross-cutting the background stratigraphy, which are interpreted as BSRs. Colour and wiggle displays are shown for the interpreted version. Also, coloured signal polarity for each BSR, compared to seafloor polarity (SEG European Polarity; increase in acoustic impedance shown as a trough with blue colour), is shown in the zoomed images (A, B, C, D and E; bottom). Blue and red triangles on the wiggle display are used to highlight troughs and peaks associated with the coloured BSR polarity. Note that BSR3 changes polarity from SW (negative) to NE (positive). Vertical black segments on the interpreted stack profile show the location of Field File Identification Numbers (FFIDs) 31692 and 31724 shown in Fig. 4.

Finally, the deepest BSR, BSR3, is characterised also by a high-amplitude reflection, which is more clearly identified on shot gathers from near-to mid-offset ranges (~3.5 km offset; channel no. 1–280; Fig. 4). Although signal polarity seems predominantly reversed to the SW-end of BSR3, it changes to normal polarity toward its NE-end (Fig. 3E). The apparent change in polarity, and the discontinuous character of this seismic reflector, leaves uncertainty in linking the SW part of BSR3 with its NE part. Thus, BSR3 could be interpreted as two different reflectors.

4. Methodology

The post-stack, time migrated seismic profile was used to pick seismic horizons, including seafloor, BSR-like reflections and other main sedimentary layer reflections. Seafloor was converted into depth assuming a constant sea-water velocity (1.49 km/s), whereas all other picked horizons were initially converted into depth using a uniform velocity gradient of 0.42 s^{-1} (Monteleone et al., 2019). Reflected travel-times, corresponding to the horizons picked on the time stacked profile, were picked on the shot gathers and used in a forward
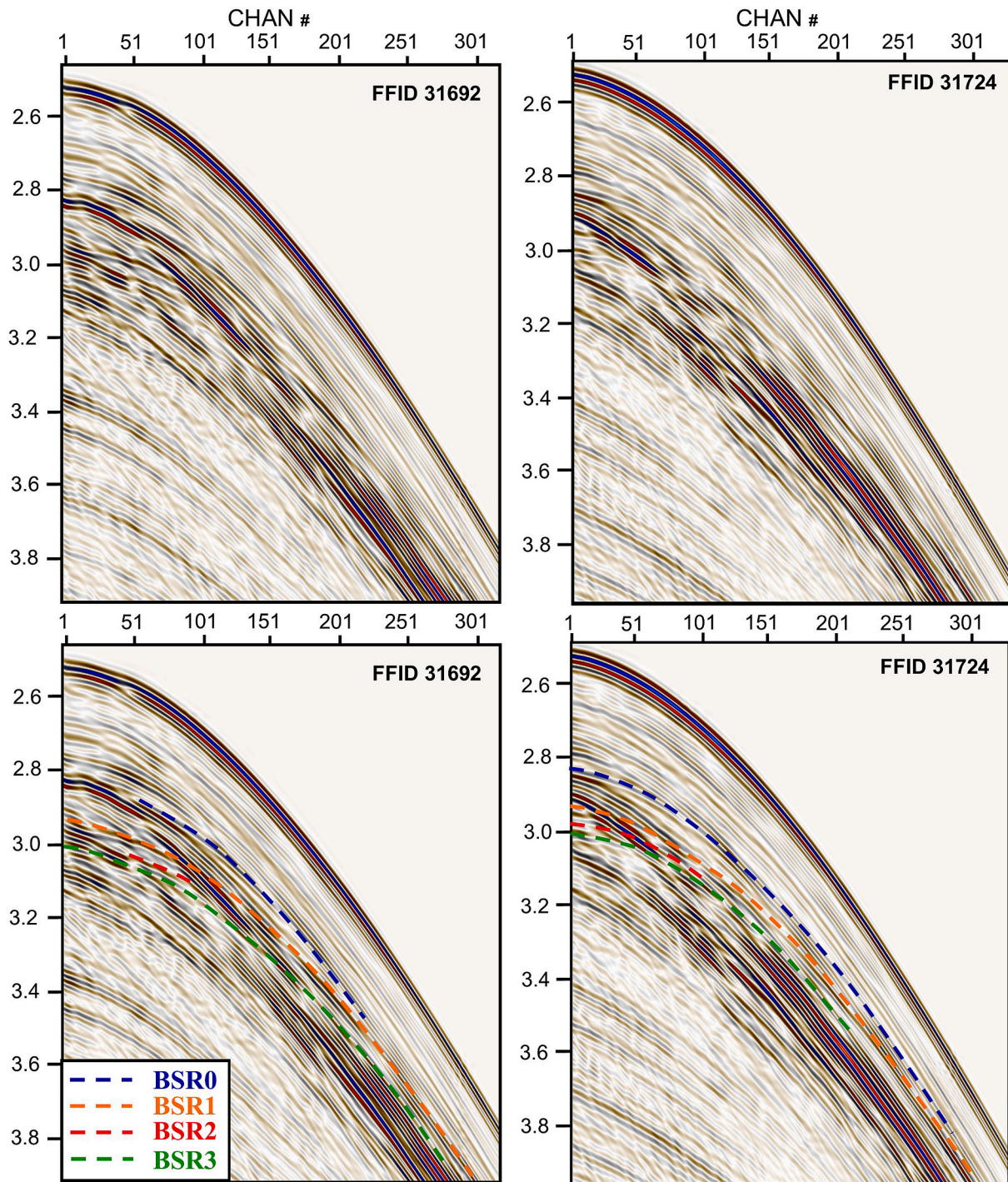
Fig. 4. Field File Identification Numbers (FFID) 31692 and 31724 (location in Fig. 3). Top) Non-interpreted shot gathers. Bottom) Interpreted shot gathers, showing an example of phase identification for all four BSRs. Offsets along the shot gathers are provided as channel number (CHAN #), where channel is a consecutive number with 12.5 m spacing.

travel-time modelling approach (Zelt and Smith, 1992) to refine the velocity model structure and layers depths.

To improve the velocity model constraints, we considered both reflected and refracted travel-times. The long-offset nature of the seismic acquisition used allows refracted signals from deep and fast stratigraphic levels to be imaged as first arrivals at far offsets. However, key velocity information would be provided by refractions from shallow stratigraphic levels located within the depth range of the BSRs, a few hundred meters below seafloor. Although reflected arrivals could be identified and picked from these levels, picking travel-times for refractions are

difficult to identify as they are obscured by earlier direct and reflected signals. Therefore, to try achieving the best result from travel-time analysis, downward continuation (Berryhill, 1979, 1984; Harding et al., 2007) was applied to streamer data (section 4.1) prior to travel-time analysis (section 4.2). The resulting velocity model combines non-downward continued reflected travel-times and downward continued reflected and refracted travel-times; this velocity model was then used to compare BSR depths with the expected BGHSZ (section 4.3), and to provide estimates of gas and hydrate saturation in sediments (section 4.4).

4.1. Downward continuation

Downward continuation is an efficient technique to extrapolate the recorded wave-field to an arbitrary surface, bringing refracted arrivals as first arrivals (Berryhill, 1979, 1984; Harding et al., 2007; Arnulf et al., 2011). It can be carried out in the frequency domain, using pre-stack phase-shift methods (Gazdag, 1978), or in the time domain (Berryhill, 1979), applying Kirchhoff's integral method and solving the wave equation using the finite difference method (Claerbout, 1976). Here we apply downward continuation to the streamer data using a pre-stack Kirchhoff integral extrapolation technique in the time domain (Berryhill, 1984), which is formulated by convolving the recorded wavefield at the streamer depth with the time lagged delta functions and summing these convolved results over all receiver locations for all shot gathers (Harding et al., 2007). The time lags are estimated by dividing the distance between the streamer locations of the shot gathers and their extrapolated positions on a different depth datum (i.e., seafloor) by a constant water velocity. In the absence of more detailed constraints on the water column velocity structure, we use a constant water velocity of 1.49 km/s assumed from stacking velocities.

The downward extrapolation has several advantages. First, it collapses the seafloor diffractions, improving the imaging condition. Second, there is the advantage of exposing more of the shallow turning refractions as first arrivals that can be accurately picked for tomography, improving vertical resolution of the resulting velocity model (Harding et al., 2016). Furthermore, the differential move-out of reflected arrivals is enhanced near to the seafloor, leading to improved velocity analysis and imaging (Arnulf et al., 2011).

Downward continuation can be performed moving both source and receivers down to the real seafloor topography or moving them to a constant datum above seafloor or below sea-level. Here, we apply a simple approach downward continuing to a constant datum below sea-level. Since our seismic profile shows seafloor depth ranges from a minimum to 1.53 km (bsl) to the NE to a maximum depth of 2.13 km (bsl) to the SW, we tested model response to different downward continuation depths. After testing, sources and receivers were extrapolated at a shallower depth of 1.6 km (bsl), which provided a trade-off between avoiding the introduction of artefacts while allowing refracted signals to become first arrivals at sufficiently closer offsets (Fig. 5).

Downward continuation was carried out in two steps: 1) the extrapolation of each set of 816 traces of the receiver gathers (corresponding to a single shot point) vertically down to 1.6 km (bsl) and, after sorting of the extrapolated shot gathers into Common Receiver Point (CRP) gathers, 2) the extrapolation of each source wave field, corresponding to 204 shots per CRP gather, to the same depth. Finally, the data were sorted back into shot gathers before travel-time analysis (Fig. 5). Further details on the pre-conditioning of the data prior to DC and testing performed for DC parameter selection are presented in section A of the supporting material.

The final output of the downward continuation shows refracted arrivals at offsets as close as 2.75 km (channel no. 220) compared to the 5.5–6 km (channel no. 440–480) within non-downward continued shot gathers (Fig. 5). The extent of the arrivals in the downward-continued data depends on the distance between the datum and the seafloor, the underlying velocity function, and local topography; therefore, the source-receiver range of reflected first arrivals changes slightly from one location to another (Arnulf et al., 2014). Whereas refracted arrivals have been improved by downward continuation, reflected arrivals are noisier in downward continued data. For this reason, non-downward-continued data were used to pick reflected travel-times, whereas downward-continued data were primarily used to pick refracted travel-times.

4.2. Travel-time analysis

For travel-time analysis, we required a code that could model both refractions and reflections, deal with a large number of layers with complex geometry defined by reflection imaging and allow integration of picks from both downward-continued and non-downward-continued data. Thus, reflection tomography and first arrival tomography codes could not be used. The widely used reflection/refraction tomography code Tomo2D (Korenaga et al., 2000) does not deal with layers constrained by reflected picks only. The JIVE 3D code (Hobro et al., 2003) can deal with such layers but struggles when many layers are present, some of which are poorly constrained. Thus, ultimately, we decided to use the forward modelling code of Zelt and Smith (1992), which with some manipulation satisfies all the above criteria.

4.2.1. Travel-time phase definition

The first stage in seismic travel-time modelling is travel-time picking
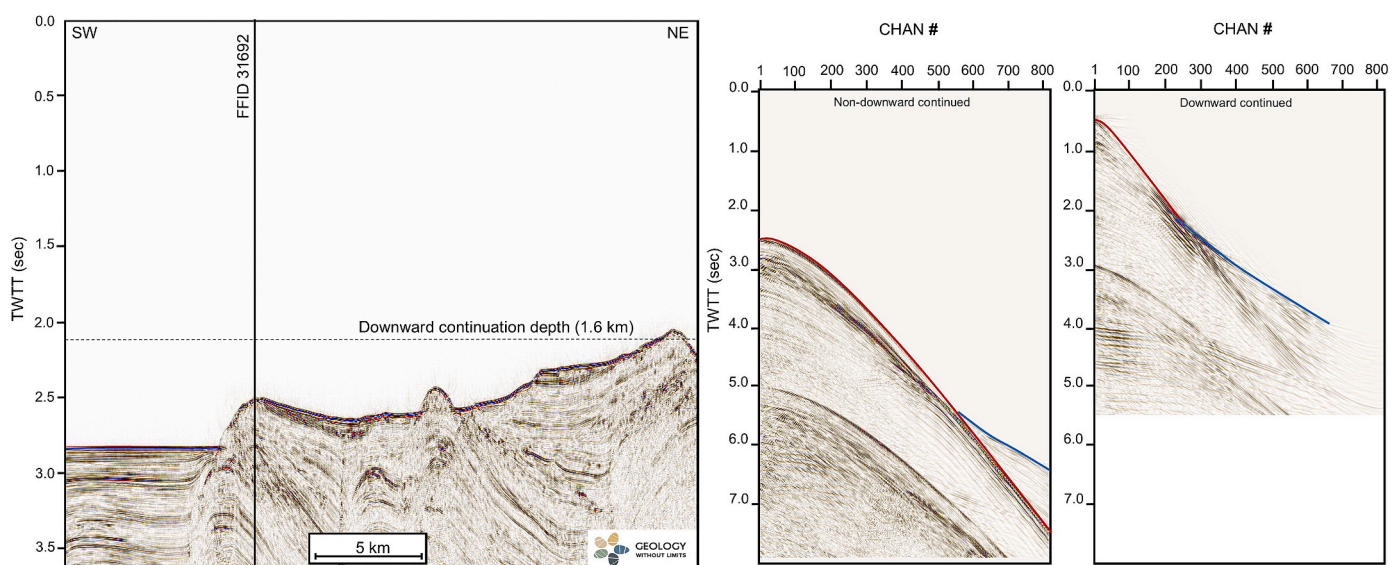
Fig. 5. Downward continuation applied to streamer data. Left) seismic profile BS-200B. The vertical line represents the location of the shot gather (FFID 31692) shown to the right. Right) FFID 31692 is compared before and after downward continuation. Seafloor reflection (red), and first arrival refraction (blue), are also shown. The comparison highlights that downward continuation allows refracted events, originally visible from ~6.8 km offset (channel 550) on non-downward continued data, to be visible as first arrivals at ~ 2.7 km offset (channel 220).

and the assignment of phase to different arrivals. Layer boundaries were defined using seismic horizons mapped in the time domain on the stack profile (Fig. 6). The depth-converted horizons were used to construct the initial layered model. Reflected arrivals (phases) corresponding to the defined layer boundaries were then picked in the non-downward-continued shot domain, where visible (shot gather in Fig. 6). Comparison with the stacked profile and with common receiver gathers was used to help identify each phase at near offsets and to provide guidance for phase recognition and picking at increasing offsets along the shot gathers. For practical reasons, we could not include every shot gather in the model. Given that travel-times showed good lateral continuity, picking every 8th shot was considered sufficient for this analysis. Phase picking was performed following the troughs (or peaks; zero-phase filter) of each reflected phase; for consistency, the same procedure was applied to refracted phases picked on downward-continued data.

A total of ten reflected phases were picked at 13 shot locations at 400 m spacing. The selected shots cover a distance from 19.45 km to 24.25 km along the 33 km-long profile (see section A of the supporting material), which includes the multiple BSR area (Fig. 6). The choice of multiple phases associated with stratigraphic reflectors beneath the BSRs is due to the geological complexity of this area, with folded structures present as steeping-dipping events often cross-cutting the BSR (Figs. 3 and 6). Thus, the choice of multiple horizons was necessary to constrain the velocity structure beneath the BSRs and within the surrounding sediments. Also, a simple model with flat, horizontal layers required unrealistic and abrupt lateral velocity variations to fit calculated and observed travel-times at the picked reflection events. Therefore, the real geometry of the reflection events was adopted for modelling (Fig. 6).

The model was then extended from the BSR area (to the NE of the profile) basinward (to the SW of the profile) to assess whether seismic velocity ranges defined in the BSRs area were representative for the shallow sedimentary section in other parts of the basin. Thus, an additional three shots from the more horizontally stratified central basin area (SW part of the profile) were included in the modelling (Fig. 6). Because of the lateral continuity of the sedimentary layers in this area, only three shot gathers at 3 km offset spacing (from 9.85 km to a 15.85

km offset along the profile) were used for phase picking (Fig. 6). At these shot locations, five phases were picked, which are laterally continuous on stack data. These layer boundaries can be followed into the NE part of the profile (within the BSR area) as boundaries 1 (seafloor), 6, 7, 8, and 9.

Downward-continued shot gathers were used mainly to pick refracted arrivals. Some reflections were also picked to check the reliability of the downward continuation procedure (Fig. 7). Three reflected phases (phase 1 - seafloor; phase 2 - BSR1; phase 3 - BSR3) and three refracted phases (phases 4, 5 and 6) were identified and picked on downward-continued shot gathers (Fig. 7; Figure B-1).

Over 27500 reflected travel-time picks were made, on both non-downward-continued and downward-continued shot gathers. Pick uncertainties were defined by looking at the dominant period of the selected travel-times, and accounted for increased uncertainty at mid-to far-offsets due to loss of amplitude, to greater dominant period, to artefacts interfering with the selected phases (especially in downward-continued data), and to other interference. Uncertainties were therefore assigned in the range of 5–10 ms, less than half of the dominant period (30 ms), to all near-normal incidence reflections picked on non-downward-continued data. An uncertainty of 20 ms was instead assigned to reflected events picked on downward-continued data, due to the deterioration in the reflected signal and the loss of high frequencies. Over 3300 refracted travel-time picks were made on downward-continued data and assigned an uncertainty from 20 ms increasing to 25 ms at far-offsets, corresponding to approximately half of a wave cycle (50 ms).

4.2.2. Travel-time modelling

Modelling was carried out in a layer-stripping approach using non-downward-continued reflected travel-time picks first, where progressively deeper phases are modelled while holding the overlying layers fixed until all data have been fitted. The resulting model was then integrated with refracted and reflected travel-times picked on downward-continued data (Fig. 8, Figure C-1 to Figure C-5). At this stage, the velocity model was adjusted where necessary, with only minor adjustments to the layer boundaries.
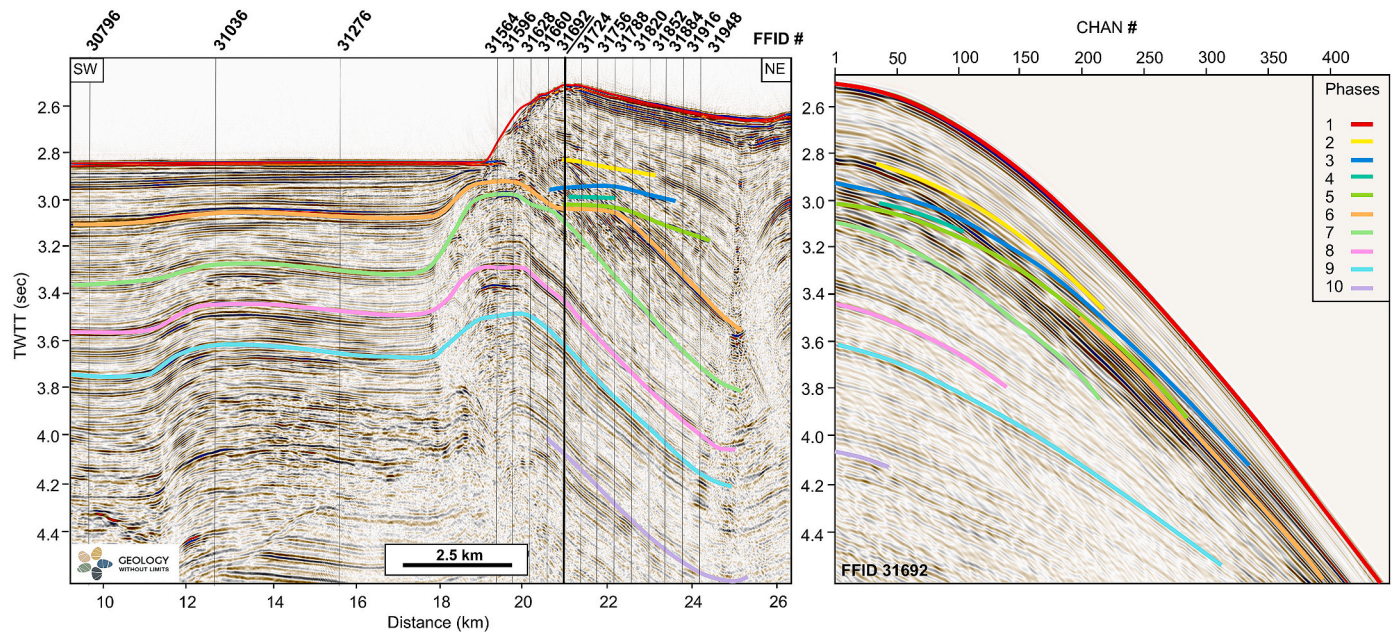
Fig. 6. Seismic reflection profile showing the interpreted seismic phases used for the velocity model construction (coloured lines), and the location of the shot gathers picked for travel-time analysis (vertical black segments). Phase 1 - seafloor reflection; phases 2, 3, 4 and 5 - BSR0, BSR1, BSR2 and BSR3, respectively; phases 6 to 10 - stratigraphic horizons beneath BSR3. The thick black segment is the location of the non-downward-continued shot gather to the right (FFID 31692) where interpreted phases are overlaid.

Fig. 7. Phase identification on downward-continued shot gather (FFID 31692). The shot location is shown in Fig. 6. Three reflected phases were identified: phase 1 - seafloor, phase 2 - BSR1 and phase 3 - 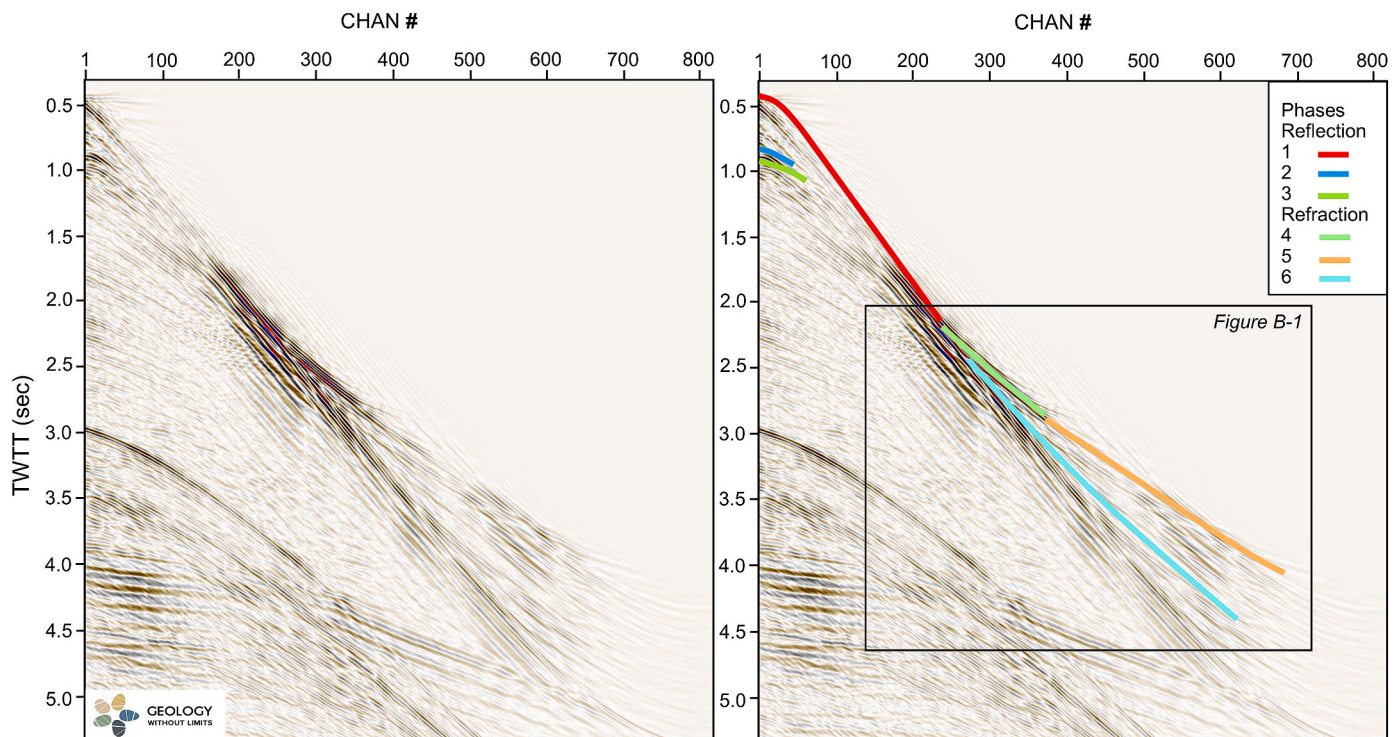BSR3. Three refractions from mid-to far-offsets were picked (phases 4, 5 and 6). Black box on the shot gather to the right refers to a zoomed image in Figure B-1 showing wiggle traces and refracted phase identification (see supplementary material).

The number and position of boundary nodes was adapted to the horizons picked along the seismic reflection profile, whereas velocity node spacing was adjusted to fit the observed data with the minimum necessary changes in depth nodes. All layers had a normalised misfit (χ^2) below 1–1.5, which was the imposed stopping criterion. Further information on the travel-time model fit and results is available in section D of the supplementary materials.

Downward continuation allowed picking of refracted signals at closer offsets, but the observed phases still come from beneath the BSRs (Fig. 8; Figures C-1 to C-5). We discuss this limitation of the downward continuation method further in section 5.1.

4.3. Modelling of the BGHSZ

We compared the depth of the interpreted BSRs with the expected depth of the BGHSZ. The GHSZ thickness below seafloor is given by the distance between the seafloor and the intersection of the temperature profile with a hydrate phase boundary (e.g., Marín-Moreno et al., 2016; Tinivella and Giustiniani, 2013). Assuming hydrostatic pore fluid pressure and steady state temperature conditions, this calculation depends upon parameters such as the bathymetry, geothermal gradient, seafloor temperature, pore-water salinity, and molecular composition of the hydrate forming gas (e.g., Sloan, 1998). Other parameters affecting hydrate stability such as pore size (e.g., Østergaard et al., 2002; De La Fuente et al., 2021) are not considered here.

Seafloor depth ranges from a minimum depth of 1.53 km to the NE, to a maximum depth of 2.13 km to the SW of the profile. We compiled temperature, salinity, and geothermal gradient data from published literature to define average parameters for the GHSZ modelling. Bathymetry is defined by the seafloor horizon picked along the time-migrated stack profile, which was converted from time to depth assuming a constant seawater velocity of 1.49 km/s. The geothermal gradient in this part of the EBSB is expected to vary between 20 and 42 °C/km, based on heat-flow measurements and other estimates

(Vassilev, 2006; Minshull and Keddie, 2010). Results from the DSDP 42B Hole 379A (see location in Fig. 1), provide a narrower range of geothermal gradients between 32 and 38 °C/km (Erickson and Von Herzen, 1978). No geothermal gradient information from industry wells in the EBSB was available for this study. Analyses of pore water samples in the same DSDP cores (i.e., DSDP 379A; Muratov et al., 1978; Ross, 1978) show that salinity decreases rapidly from ~2.23 wt % at the seafloor (Özsoy and Ünlüata, 1997) to ~ 0.2–0.5 wt % in shallow sub-seafloor depths (Calvert and Batchelor, 1978), as geochemical conditions within the sediments change to lacustrine (e.g., Manheim and Schug, 1978; Riboulot et al., 2018; Riedel et al., 2020). Within 25 to 350 m-deep sediments the pore-water salinity is low at about 0.5% wt, caused by the dominant fresh-water stages during Quaternary deposition (Manheim and Schug, 1978). These correspond to limnic conditions that occurred during sea-level low-stands, when Mediterranean seawater could not pass the Bosporus inlet and the Black Sea was isolated (Manheim and Schug, 1978).

A seafloor temperature of 9 ± 0.1 °C is well constrained by numerous studies and is generally uniform across the whole basin (Degens and Ross, 1974; Xing and Spiess, 2015; Ker et al., 2019; Vassilev, 2006). Finally, based on the analysis of methane isotope signatures from cores and seeps, the primary hydrate-forming gas composition for the Black Sea hydrate is considered to be 99.1–99.9% methane (e.g., Ginsburg and Soloviev, 1998; Vassilev and Dimitrov, 2002; Poort et al., 2005; Merey and Sinayuc, 2016; Zander et al., 2020; Chazallon et al., 2021). Furthermore, gravity corer data from the Batumi region of the EBSB have shown that the recovered gas hydrate samples contain 99.96% methane gas (Heeschen et al., 2011). Therefore, we focused on Structure I methane hydrate-gas composition for our modelling of the gas hydrate stability field; nevertheless, we cannot completely rule out the presence of thermogenic gasses as those have been reported by some studies from the central Black Sea and along the northern upper slope (e.g., Merey, 2017; Limonov et al., 1997; Kruglyakova et al., 2004; Mazzini et al., 2004).
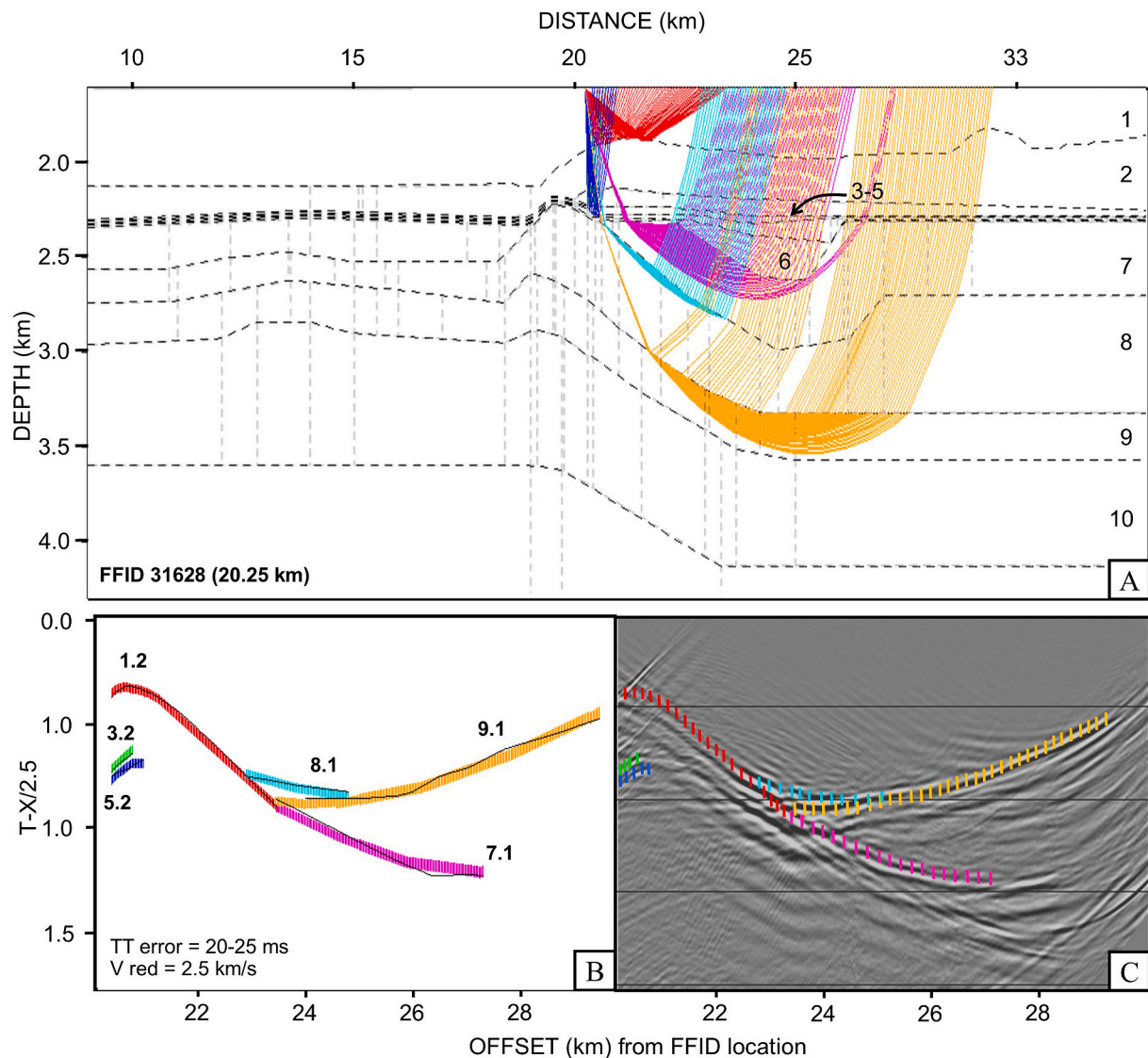
Fig. 8. Travel-time analysis on a representative downward-continued shot gather (FFID 31628). (A) Plot showing the structure of the model and the velocity node positions (the corresponding velocity field is shown in overlay in Fig. 9) initially defined by layer stripping approach using reflected travel-time phases picked on non-downward-continued gathers. Point-to-point raytracing of every 5th pick is also shown and belongs to refracted and reflected phases picked on FFID 31628, used to complement model definition. Phases 1, 2 and 3 in the modelling represent reflections from layer 1 (seafloor), layer 3 (BSR1) and layer 5 (BSR3), respectively (see Fig. 6). Three refractions, phases 4, 5 and 6, are associated with layers 7, 8 and 9, respectively. (B) Observed and calculated travel-times are compared. (C) Vertical bars mark every nth observed travel-time along with their uncertainties; real shot gather is shown. A reduction velocity (V red) of 2.5 km/s is used.

Based on the compiled data, we consider a 100% methane hydrate phase boundary (Moridis, 2003), 0.5 % wt pore water salinity (e.g., Soulet et al., 2010; Riboulot et al., 2018; Bohrmann et al., 2018; Bialas et al., 2020), seafloor temperature of 9 °C (e.g., Degens and Ross, 1974; Vassilev and Dimitrov, 2002), geothermal gradient varying between 20 and 42 °C/km (e.g., Erickson and Von Herzen, 1978; Vassilev, 2006; Minshull and Keddie, 2010), water density of 1030 kg/m³, and hydrostatic pressure. As Moridis (2003) only considers methane hydrate stability curve from pure water, we use Dickens and Quinby-Hunt (1994) relationship (their eq. 7) to convert the methane hydrate stability curve for pure water to 0.5 % salinity.

4.4. Effective-medium modelling

Knowledge of the compressional (V_P) and shear (V_S) wave velocity can be used to estimate gas hydrate and free gas content in the pore space (e.g., Ecker et al., 1998; Jakobsen et al., 2000; Waite et al., 2009). Higher velocities than those expected for water-filled, normally

compacted marine sediments within the GHSZ can often be attributed to the presence of gas hydrate (e.g., Chand et al., 2004). The presence of small concentrations (i.e., only few percent) of free gas in the pore space can attenuate the propagation of seismic waves and reduce considerably the P-wave velocity, and thus, this can be used to define gas content in low-velocity zones (e.g., Singh et al., 1993).

Here we used the Hydrate-Bearing Effective Sediment (HBES) model described by Marín-Moreno et al. (2017). The model mathematically represents the concept of hydrate-bearing sediment being an effective medium comprised by sediment grains, solid hydrate, water, and gas. It is based on the Biot-Stoll formulation (Biot, 1956; Stoll and Bryan, 1970) and predicts V_P and V_S, and P- and S-wave attenuation (or intrinsic attenuation) of hydrate-bearing sediments (Mavko et al., 2009). In the HBES model, the hydrate's habit is considered as either pore-floating, cementing hydrate at grain contact, or cementing hydrate enveloping the grains (Ecker et al., 1998, 2000) and load-bearing (Sahoo et al., 2019). Different hydrate habits can affect V_P and V_S differently and, generally, the presence of pore-floating hydrate results in small changes
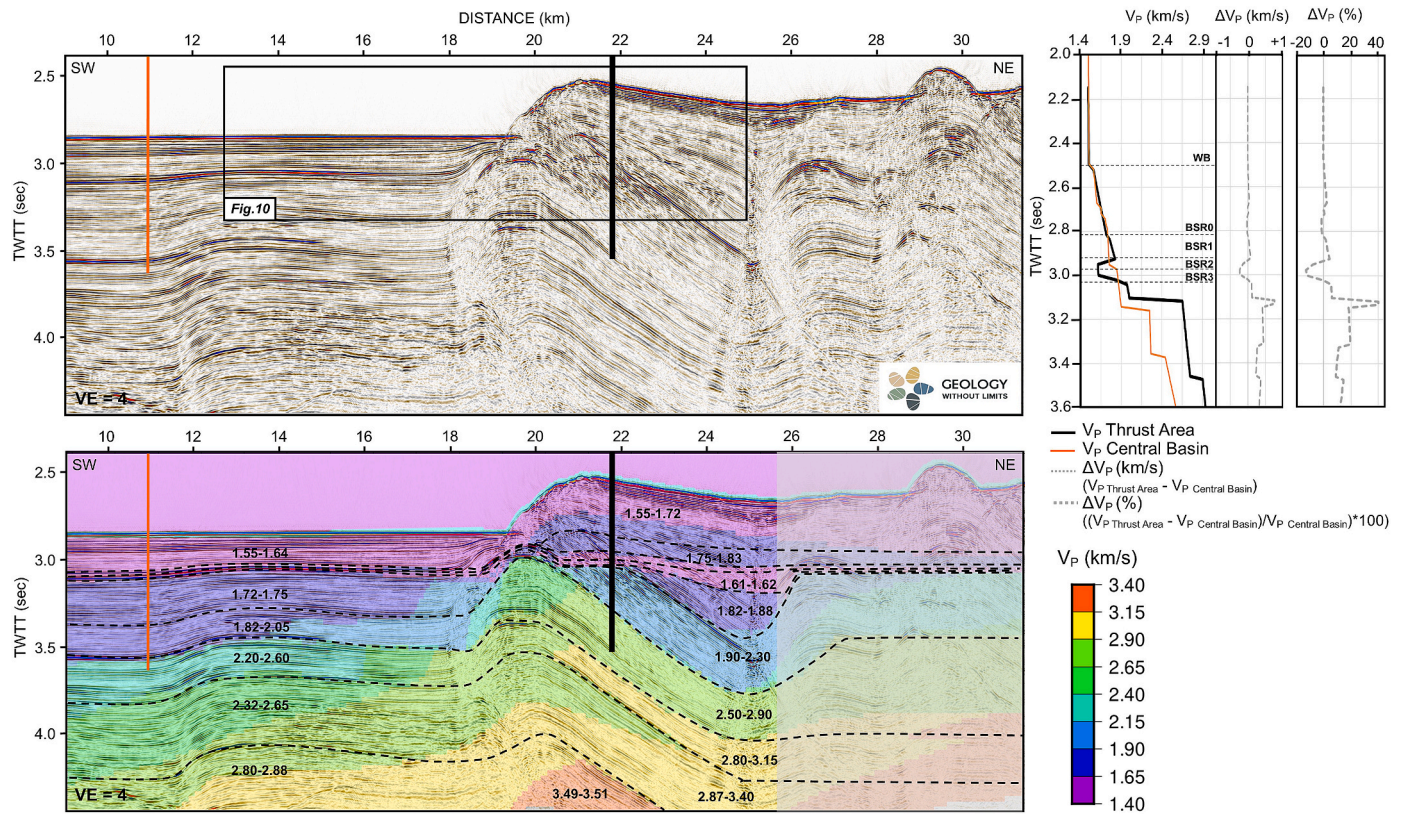
Fig. 9. Post-stack time-migrated profile of the seismic data used for velocity modelling (top), and the 2D velocity model resulting from the combined reflected and refracted travel-time analysis overlaid on top of the seismic section (bottom). Modelling of the NE portion of the profile (shaded area) was complicated by the presence of closely spaced folds and dipping layers not properly resolved by seismic imaging; therefore, we did not focus on constraining the complex geology in this portion of the profile but rather in better constraining layers between 9.85 km and 24.25 km distance. The thick orange and black lines on the seismic sections show the location of the 1D velocity profiles (inset to the top right). Note that the 1D velocity profile for the central basin was shifted up to match the water bottom (WB) at the thrust area 1D velocity profile. V_P values for the central basin and the thrust area are in displayed in km/s. The absolute delta between the two V_P trends is shown, along with the delta % considering V_P from the central basin as reference value (grey dotted lines). The black box in the top section marks the zoomed part shown in Fig. 10.

in elastic wave velocities, whereas load-bearing and cementing hydrate-bearing sediments show significantly higher V_P and V_s than those of the host sediment (Priest et al., 2009; Dai et al., 2012). This different velocity response depending on hydrate habit is represented in the HBES model by considering that pore-floating hydrate only modifies the bulk modulus of the pore fluid, whereas cementing hydrate increases both the bulk and shear moduli of the sediment (Ecker et al., 1998, 2000).

Here, the physical properties of the composite sediment are modelled by mixing the various components in different ways (see section 4.4.1). To quantify the saturation of the different components that can explain the V_P obtained from travel-time analysis, we fix the shear and bulk moduli of the mineral grains, methane hydrate, methane gas and brine and test different fractions of these components (the shear modulus of the fluids is assumed to be zero). For simplicity, we do not consider cases in which free methane coexists with methane hydrate, although we recognise that hydrate and gas can co-exist (e.g., Liu and Flemings, 2006; Sahoo et al., 2018). We therefore consider two models, one with variable amounts of methane hydrate and brine in the pore space, and the other with variable amounts of methane gas and brine. We assume that any methane gas present has a uniform distribution in the pore space. This assumption maximises the effect of gas on velocity, giving a lower bound on gas content. We compared the calculated V_P from the HBES model with the observed V_P from travel-time modelling at two locations, one in the flat-lying sediments of the central basin and the other in the BSR area. Sediment velocities in the central basin appear lower than towards the zone where BSRs are interpreted, and no velocity

inversion is observed; thus, we consider them to be representative for background V_P ranges (i.e., non-hydrate-bearing sediments). This comparison was done at stratigraphic depths of ~258, 360 and 438 mbsf, corresponding to BSR0, BSR1 and BSR3, respectively. Given the small variation in V_P between the layers above and below BSR2, BSR2 depth was not input as a relevant boundary into the effective-medium modelling. In the following we only present V_P from the HBES model as this is the parameter constrained by travel-time analysis.

4.4.1. Modelling parameters

The youngest sediments in the EBSB have been sampled by gravity cores, onshore geological mapping (i.e., NE Turkey) and existing well control. Sediment cores obtained during the DSDP Leg 42B in 1975 in the eastern-central Black Sea (Hole 379A) and at the entrance of the Bosphorus in the WBSB (Holes 380, 381) provide valuable information on the shallow sediment composition in the Black Sea (Muratov et al., 1978; Ross et al., 1978) (well locations in Fig. 1). Sediment composition information from these borings has been used by previous studies in the Black Sea to quantify gas hydrate and free gas saturation in sediments where BSRs have been identified (e.g., Lüdmann et al., 2004; Zillmer et al., 2005).

Here, we use previous estimates of the physical parameters of the solid grains/minerals (i.e., shear and bulk moduli, K_s and G_s, density, ρ_s) from Zillmer et al. (2005), that assumed a mineral composition of 60% clay, 20 % sand (quartz) and 20% Ca–Mg carbonate lithology. Based on shear and bulk moduli, and density values presented by Mavko et al. (2009), Zillmer et al. (2005) estimated average values of

$K_s \approx 32 \pm 5$ GPa, $G_s \approx 16$ GPa and $\rho_s \approx 2630 \pm 50$ kg/m³. Based on the estimated ρ_s, these authors calculated a porosity (ϕ) decrease between the seafloor and 205–270 mbsf from 78 ± 1% to 57 ± 7%. Other studies have reported porosities of ~60% for the shallow sediments of the Black Sea, decreasing down to 50% at sediments around 150 mbsf (e.g., Vassilev, 2006; Riboulot et al., 2018; Merey, 2017). At DSDP Hole 379A, the ~70% porosity within shallow sediments decreases to 38% at ~350 mbsf depth (Ross et al., 1978). We therefore considered a porosity range of 30 to 50–60% for the deepest (~600 mbsf) to the shallowest (~258 mbsf) modelling depth used in this study (Tables 1 and 2).

Pore pressure and temperature are needed to calculate the density, viscosity, and bulk modulus of the fluids (methane gas and liquid water) and effective pressure is required for the calculation of the dry moduli in the presence of pore-floating hydrate (see Marín-Moreno et al., 2017). Hence, at the four BSR depths below seafloor (258 m, BSR0; 360 m, BSR1; 438 m, BSR3; Table 1), we calculated pore pressure (P_p), confining pressure (P_{conf}) and effective pressure ($P_{eff} = P_{conf} - P_p$). In these calculations we assumed hydrostatic conditions, grain and water densities of 2630 kg/m³ and 1030 kg/m³, respectively, and an average hydrate-free porosity of 50% (this porosity value was used to estimate sediment density for the effective pressure calculation). The imposed depth uncertainty ($\Delta Z_s = \pm 10$m) comes from estimates at the layer boundaries using travel-time sensitivity analysis (section D of supplementary information) and used to derive pressure uncertainty (Table 1). For the temperature, we used a seabed temperature of 9 °C (Degens and Ross, 1974), and an average geothermal gradient of 31 °C/km was defined based on the range considered in this study (20–42 °C/km) (e.g., Erickson and Von Herzen, 1978; Vassilev, 2006), with an imposed uncertainty $\Delta T/km = \pm 11$ °C/km (Table 1). For consistency with the modelling of the GHSZ presented above, we consider a salinity of 0.5 wt % and pure methane gas and hydrate. The pore-water salinity (s) is specified based on representative values for the EBSB. Physical parameters for the gas hydrate solid phase occupying the pore space assume

Table 1

Test conditions: confining pressure (P_{conf}), pore pressure (P_p), effective pressure ($P_{eff} = P_{conf} - P_p$) and temperature (T) of sediments at the chosen stratigraphic depths. Imposed uncertainties include: ΔZ_s = uncertainty in stratigraphic depth from travel-time analysis; ΔTs = uncertainty in sediment temperature; $\Delta T/km$ = uncertainty in geothermal gradient value assuming an average value of 31 °C/km within the range of 20-42°C/km; $\Delta \phi$ = uncertainty in sediment porosity; $\Delta \rho_s$ = uncertainty in solid grain density. Derived uncertainties are: $\Delta \rho$ = uncertainty in bulk density of the sediment (calculated as $\rho = \rho_s (1 - \phi) + \rho_w \cdot \phi$); ΔP_p = uncertainty in pore pressure calculated as $P_p = \rho_w \cdot g \cdot Z_s$; ΔP_{conf} = uncertainty in confining pressure calculated as $P_{conf} = \rho \cdot g \cdot Z_s$; ΔV_P = uncertainty in seismic velocity estimate.

	Depth (mbsf)	P_p (Pa)	P_{conf} (Pa)	P_{eff} (Pa)	T (°C)
BSR0	258	2.6×10^6	4.6×10^6	2×10^6	17
BSR1	360	3.6×10^6	6.5×10^6	2.9×10^6	20
BSR3	438	4.4×10^6	7.9×10^6	3.5×10^6	23
-	600	6.1×10^6	1.1×10^7	4.9×10^6	28
Imposed uncertainty values					
ΔZ_s			±10 m		
ΔTs			±3–5 °C		
$\Delta T/km$			±11 °C/km		
$\Delta \phi$			±5%		
$\Delta \rho_s$			±0.05 g/cm³		
Derived uncertainty values					
$\Delta \rho$			±0.105 g/cm³		
ΔP_p			±0.1 × 10⁶ Pa		
ΔP_{conf}			±0.4-0.7 × 10⁶		
ΔV_P			±27–37 m/s		

Table 2

Input parameters for the HBES model [[1]Best et al., 2013;[2]Helgerud et al., 2009;[3]Setzmann and Wagner, 1991;[4]Zillmer et al., 2005;[5]Ecker et al., 2000;[6]Millero et al., 1980]. Note: we present the most relevant modelling parameters for reproducibility purposes. Some of these parameters, e.g., fluid pressure and fluid flow related parameters, are relevant primarily for attenuation and velocity dispersion analysis which is not within the scope of this work. For more detailed information refer to Marín-Moreno et al. (2017).

Component properties	
Hydrate bulk modulus (K_H)[1]	7.9×10^9 Pa
Hydrate shear modulus (G_H)[1]	3.3×10^9 Pa
Hydrate Poisson's ratio (v_H)	0.32
Hydrate density (ρ_H)[2]	925 kg/m³
Methane bulk modulus (K_{CH_4})[3]	K_{CH_4} (P_p, T) [Pa]
Methane density (ρ_{CH_4})[3]	ρ_{CH_4} (P_p, T) [kg/m³]
Solid composition[4]	60% clay, 20% quartz, 20% Ca–Mg
Solid grain bulk modulus (K_S)[4]	32×10^9 Pa
Solid grain shear modulus (G_S)[4]	16×10^9 Pa
Solid grain Poisson's ration (v_S)[4]	0.29
Solid grain density (ρ_S)[4]	2630 kg/m³
Solid grain diameter (d_S)	1×10^{-5} m
Solid grain coordination number (n)[5]	9
Water bulk modulus (K_w)[6]	K_w (P_p, T) [Pa]
Water density (ρ_w)[6]	ρ_w (P_p, T) [kg/m³]
Water salinity (s)	0.5 % wt
Parameters	
Porosity without hydrate (ϕ)	0.3–0.6
Critical porosity (ϕ_c)[1]	0.38

values for pure methane (structure I) hydrate, which is observed to occur more widely in nature (e.g., Kvenvolden, 2000) and in the Black Sea (Michaelis et al., 2002; Poort et al., 2005; Bialas et al., 2020; Merey and Sinayuc, 2016).

Reference values used for the calculations, their imposed uncertainties, and their propagation in calculated velocities (ΔV_P) are shown in Table 1 and other relevant input parameters for the HBES model are presented in Table 2.

5. Results and interpretation

5.1. Benefits and limitations of downward continuation

The long-offset nature of the seismic data used in this study allows refracted arrivals to be imaged at far offsets. Streamer data preconditioning can help to improve this travel-time information, making it comparable with a seafloor or near-seafloor refraction experiment (e. g., Harding et al., 2007; Henig et al., 2012). We therefore tested the ability of the downward continuation technique to enhance refracted arrivals and thereby constrain velocity information within the top few hundred meters of sediments, focusing on where multiple BSRs have been identified.

Downward continuation improved the first arrival refraction, collapsing the seafloor reflection towards zero offset and bringing out refractions from shallower structures as first arrivals at nearer offsets. However, downward-continued data also contain strong linear artefacts at near offsets, which come before the first arrivals. These artefacts limited the refracted arrival offsets that could be used for travel-time analysis. Furthermore, we were not able to recover refracted information between the multiple BSRs. This may be due to (i) the limited vertical spacing between the BSR seismic phases and (ii) their shallow sub-seafloor depth meaning that, although refractions may be generated at such levels, they will not appear as first arrivals on shot gather but they are most probably masked by other refractions from deeper and faster layers (e.g., Qin and Singh, 2018). These deeper refracted arrivals would still bear some information on the velocity structure of the layers they have travelled through; however, the impact of these layers on the deeper refractions travel-times may be minor considering their relatively small vertical thickness. These factors limit the downward

continuation technique when applied to shallow stratigraphic targets, thus impacting refracted travel-time analysis; however, the integration of refracted travel-times provided further support for the velocity model defined using reflected travel-times and better constrained the deeper stratigraphic layers.

Another element that affected our results is the geological complexity of the study area. This complexity resulted in noise and artefacts being introduced during downward continuation and also limited our ability to sample laterally continuous refracted and reflected events across shot gathers. Finally, since refracted arrivals are not generated by low-velocity zones, refracted travel-times provide little constraint on gas-bearing zones. For all these reasons, reflected travel-times were essential for velocity model construction and definition, whereas only few refracted arrivals could be used to improve the velocity field. Nevertheless, these refractions allowed us to check model consistency and to better constrain the lateral variation of the velocity field, as their travel-times bear information about the velocity structure of shallower layers.

5.2. Velocity model

Based on travel-time analysis, we constrain the depth of the picked seismic phases (Fig. 6) and the velocity structure between them (Fig. 9). BSR0, BSR1, BSR2 and BSR3 are inferred at an average depth of 258, 360, 395 and 438 ± 10 mbsf, respectively, where seafloor depth is between 1976 m and 1868 m along the extent of the interpreted BSRs. Thus, we assumed an average seafloor depth of around 1920 m for this analysis. Note that we consider V_P trends rather than interval velocities (V_{INT}) as they represent better how seismic velocities change within each layer and, consequently, they provide a better understanding of how physical properties of sediments change with depth within each layer. V_P increases from 1.55 km/s to 1.72 ± 0.02 km/s between seafloor and BSR0, from 1.75 km/s to 1.83 ± 0.01 km/s between BSR0 and BSR1, and a V_P decrease from 1.83 km/s to 1.61 ± 0.03 km/s is modelled beneath BSR1. This low-velocity zone, which includes BSR2, is defined as a 70-80 m-thick layer bounded by BSR1 and BSR3 at its top and bottom, respectively. Within the low-velocity zone, the reduction in V_P of about 12% with respect to the V_P at BSR1 may indicate the presence of free gas. V_P then increases rapidly underneath BSR3, starting from values of 1.82–1.90 km/s (Fig. 9).

The velocity model shown in Fig. 9 is poorly constrained to the NE part of the profile, where the complexity of the compressional tectonics and our ability to pick travel-time events consistently across shot gathers limited modelling of travel-time arrivals. Thus, the layer depths and velocity structure of the travel-time model in this area are assumed to be laterally continuous with the layers defined in the area of the multiple BSRs (Fig. 9). To the SW of the profile, within the almost horizontal layering of the central basin, modelling is better constrained and layer boundaries can be traced in lateral continuity with the ones defined in the BSRs area (Fig. 9). However, at the front of the compressional folding marking the transition from the BSRs area to the central basin domain, seismic events are also poorly imaged. As a result, this area has also to be considered poorly constrained in terms of the defined velocity model.

We focused on the definition of the shallow sediment velocity structure for the area where BSRs are identified (NE) and, as a comparison, for the sediments at similar sub-seafloor depths in the central basin (SW) (Fig. 9). Although hydrate-related BSRs may also be present in the central basin, the lack of low-velocity zones suggests the absence of gas trapped beneath a BGHSZ; thus, we consider sediments in the central basin area to represent background values to which compare observations from the multiple BSRs area. These two areas show seismic velocities with different trends. Sediments up to 258 mbsf in the central basin have a V_P range of 1.55–1.64 km/s, so V_P values lower than the range of 1.55–1.72 km/s modelled in sediments above and at BSR0. Similarly, sediments up to 360 mbsf in the central basin have a V_P range

of 1.72–1.75 km/s, also with V_P values lower than the range of 1.75–1.83 km/s modelled above and at BSR1. Furthermore, the low-velocity zone modelled between BSR1 and BSR3 is not matched by any low-velocity zone in the central basin, where sedimentary velocities increase monotonically with depth. The presence of higher velocities in sediments between the seafloor and the imaged BSRs may indicate lithological changes, enhanced compaction and/or the presence of hydrate-bearing sediments. The lower velocities of sediments in the central basin are considered to be representative of background values with no hydrate in sediments.

Similar velocity trends within the shallow sediments are observed in Scott et al.'s (2009) tomographic seismic experiment, and in well data (Ross et al., 1978; Muratov et al., 1978). Based on a travel-time analysis in the central-SW part of the EBSB, Scott et al. (2009) found that the seismic velocity in shallow sediments steadily increases with depth by a vertical gradient of ~0.7 s^{-1}. Generally, the velocity gradient expected for shallow sub-seafloor sediments dominated by a shale lithology is ~0.55 s^{-1} and by a sand lithology is ~1–1.15 s^{-1} (Japsen et al., 2007). Scott et al. (2009) interpreted their ~0.7 s^{-1} gradient to suggest a shale-dominated lithology, in agreement with the DSDP Hole 379A lithostratigraphy (Ross, 1978). Given the lateral uniformity of sediments across the whole basin, we assume the same lithology (and velocity gradient) in our study area; then, we compare the velocity trends observed in sediments above BSR1 with the expected velocity trends assuming standard velocity gradients for shale and sand lithology (Japsen et al., 2007), and with the expected velocity trends assuming the intermediate shale gradient estimated by Scott et al. (2009). The same comparison is also done for the velocity trend estimated within shallow sediments in the central basin (Figs. 9 and 10).

The comparison between V_P profiles shows that shallow sediment velocities in the central basin have a similar gradient to that estimated by Scott et al. (2009), which is representative of a shale-dominated lithology (Fig. 10). Sediments in the BSR area are instead characterised by higher V_P gradients than those expected for a shale-dominated lithology. Sediments above BSR0 show a velocity gradient similar to that of sand-dominated lithology (Japsen et al., 2007), and sediments between BSR0 and BSR1 have an even higher gradient (Fig. 10). Below BSR1, the low-velocity zone represents another velocity anomaly (Figs. 9 and 10). Although from travel-time analysis we cannot determine the internal structure of the low-velocity zone, its thickness and mean velocity are well constrained by travel-times from a reflector marking its base.

5.3. Modelling of the BGHSZ

The comparison between the depths of the BSRs, calculated by travel-time analysis, and the calculated BGHSZs shows that a geothermal gradient of 38 °C/km provides the best fit with the depth of BSR0. The BSR1 depth is instead best fit by geothermal gradients between 26 and 30 °C/km. Lower geothermal gradients need to be assumed for the deeper BSRs (BSR2 and BSR3) (Fig. 11).

Parameters such as salinity, seafloor temperature and hydrate-forming gas composition are well-constrained across the Black Sea, and they are not expected to vary in this area. The main source of uncertainty is then the geothermal gradient. Hole 379A provides some constraint on the expected geothermal gradient in the EBSB, showing values between 32 and 38 °C/km (Erickson and Von Herzen, 1978); however, measurements from geothermal stations across the whole Black Sea show a high degree of location-specific variation in the geothermal gradient (Vassilev and Dimitrov, 2002). Our profile lies in an area with measured geothermal gradients around 42 °C/km or higher; these high gradients may be linked to the tectonic setting and to fluid flow through the deep-rooted fault systems dominating the folded sediments of the Tuapse Trough (Vassilev, 2006).
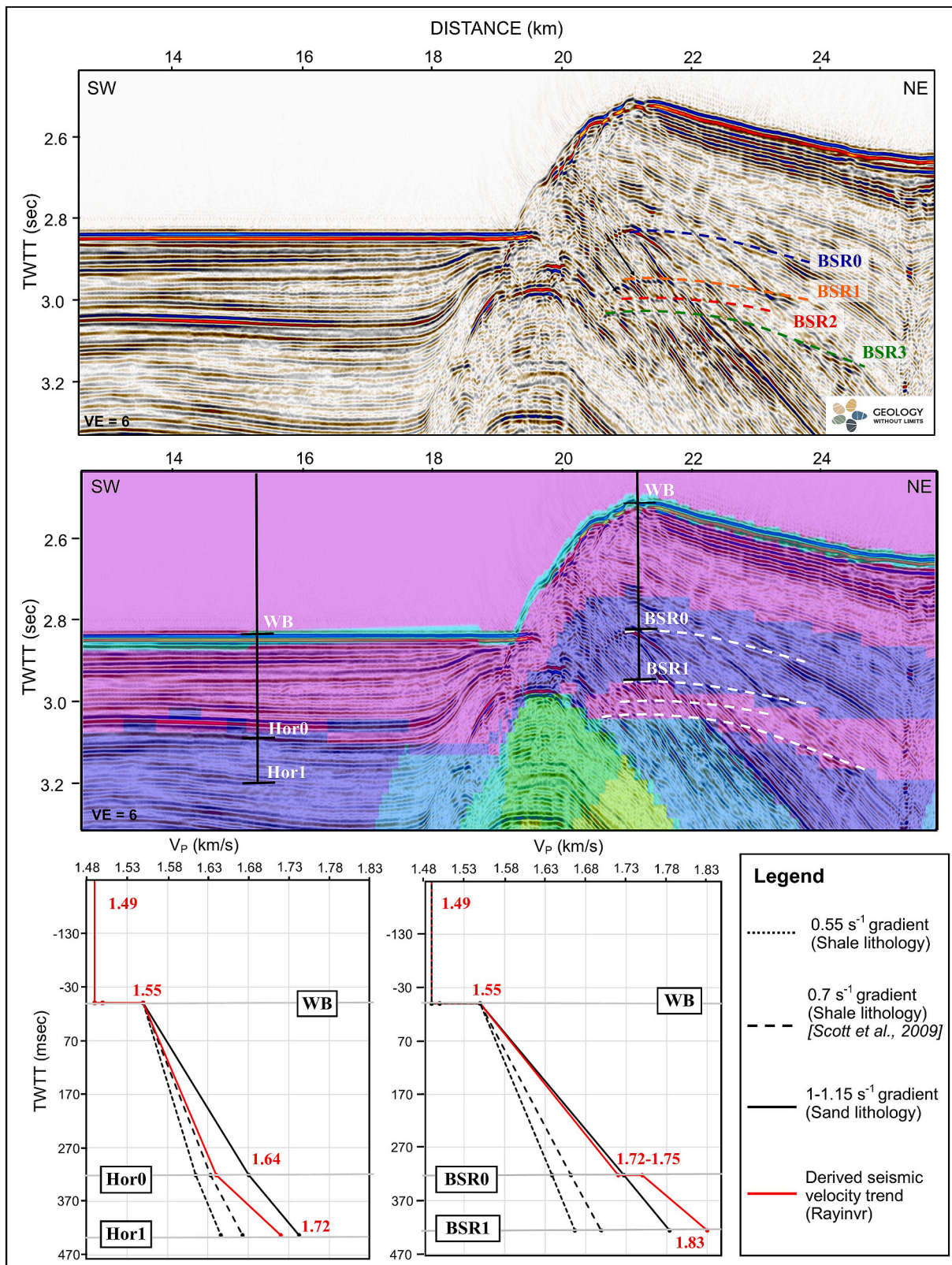
Fig. 10. Comparison between seismic velocity trends (V_P) for the shallow sediment (as derived from modelling results) in the central basin and in the BSR area, from seafloor (WB) down to ∼ 260 mbsf (Hor0) and ∼360 mbsf (Hor1), and from seafloor (WB) down to BSR0 and BSR1, respectively. Note that the vertical scale for the velocity plots at the bottom of the figure are expressed in milliseconds below seafloor (positive values) to make plots comparable. V_P trends are also calculated assuming velocity gradients expected for shale (0.55 s^{-1}) and sand (1.1 s^{-1}) dominated lithologies (Japsen et al., 2007), and the velocity gradient estimated by Scott et al. (2009), which was interpreted as representative for the shale lithology of the Black Sea shallow sediments (0.7 s^{-1}).
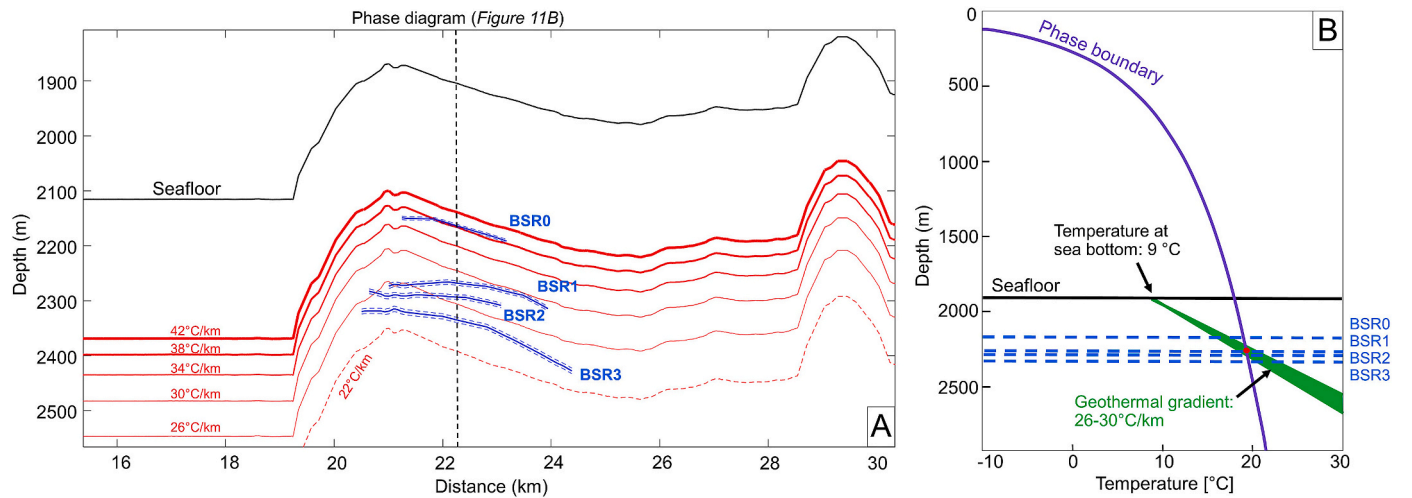
Fig. 11. A) Results from modelling the BGHSZ assuming 100% methane gas composition, 0.5% wt pore-water salinity, 22–42 °C/km geothermal gradient, and 9 °C near seafloor temperature. Black line represents seafloor depth obtained from seismic data; continuous blue lines are seismic BSR depths, and dashed blue lines show BSR depth uncertainty for a ±20 m/s velocity variation estimated from travel-time analysis; red lines represent the calculated BGHSZ. B) Phase diagram illustrating the stability conditions of methane hydrates at the location depicted in A and highlighting that BSR1 corresponds to the BGHSZ assuming a geothermal gradient between 26 and 30 °C/km. Vertical axis is depth below sea-level.
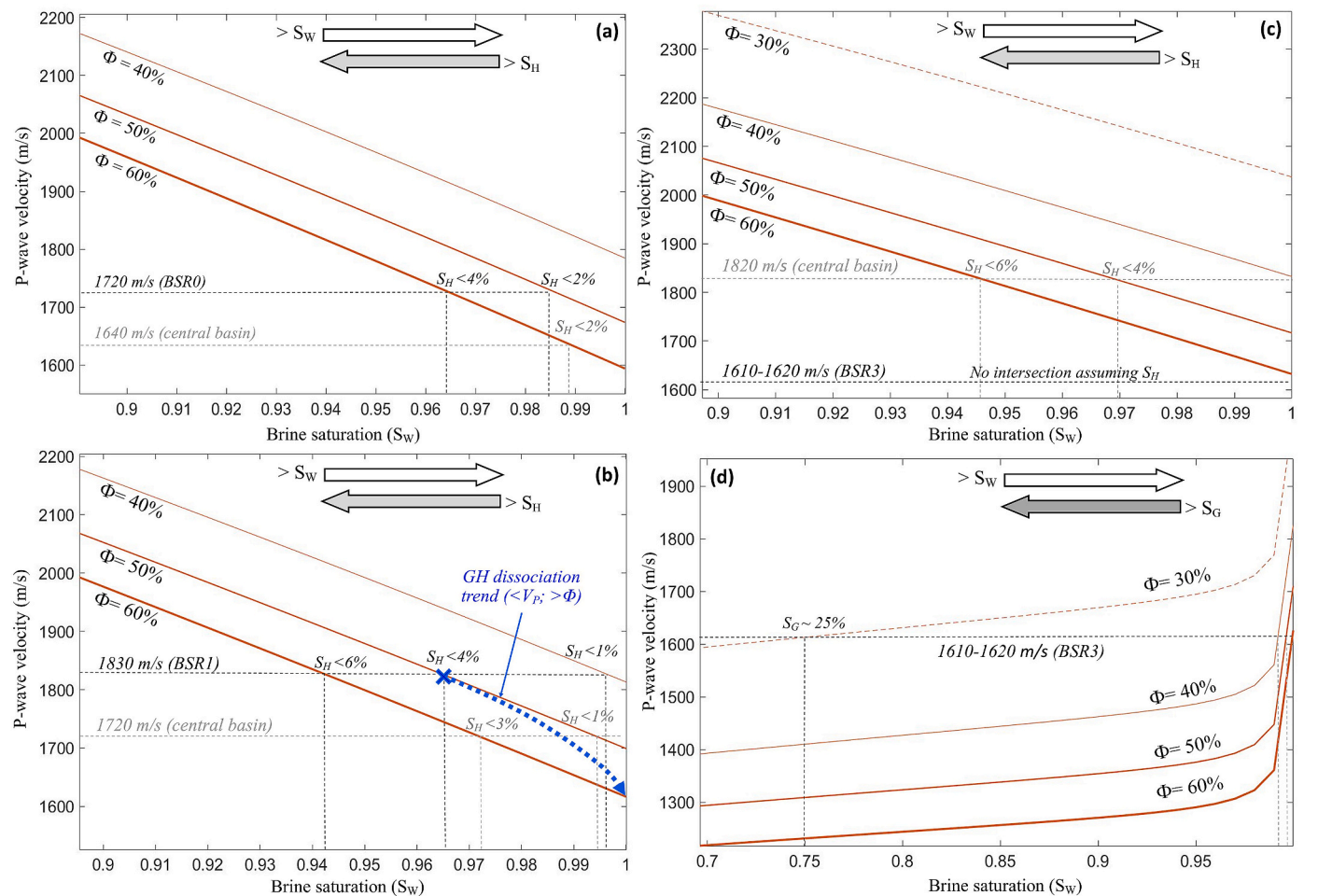

Fig. 12. Plot of V_P trends at different percentages of brine saturation (S_w), hydrate saturation (S_H) or gas saturation (S_G) in the pore space, and as function of porosity (φ). Arrows displayed at the top of each plot highlight increasing S_w versus S_H (a, b and c) and S_w versus S_G (d) trends. A S_w of 1 means fully water-saturated sediment. For a $S_w < 1$, a percentage of the pore space is made up of either hydrate (a, b and c) or gas (d). V_P trends are shown at (a) 258 mbsf, (b) 360 mbsf, (c)-(d) 438 mbsf. V_P values are summarised in Table 3. Blue arrow in (b) highlights the expected trend of V_P and φ values following hydrate dissociation; V_P decreases as result of an increase in φ possibly combined with some of the released gas trapped in the system.

5.4. Effective-medium modelling

We used the effective-medium modelling approach described by Marín-Moreno et al. (2017) to calculate V_P and compare it with the V_P obtained from travel-time analysis (hereafter named as *observed* V_P). We model depths associated with main changes in V_P, which are related to the depth of the identified BSRs. Similar sub-seafloor depths are assumed in the central basin. This comparison allows to define which ranges of hydrate (S_H) or gas (S_G) saturation in the pore space can explain the observed V_P. Hydrate habit has a strong influence on the physical properties of hydrate-bearing sediments (e.g., Spangenberg et al., 2014), with cementing hydrate highly increasing V_P even at low (below 1%) hydrate saturation. Here, V_P values calculated assuming cementing hydrate were much higher and not comparable with the observed V_P in our study area. Thus, we assumed a pore-floating hydrate habit.

Table 3
Tables showing values of calculated V_P (in m/s) obtained at different stratigraphic depths for different porosity (%) and S_H (or S_G) (%). V_P ranges highlighted show the match with the observed V_P.

258 mbsf (central basin)

S_H (%)	φ 40	φ 50	φ 60
0	1782	1671	1592
1	1819	1709	1630
2	1856	1746	1667
3	1893	1782	1704
4	1929	1819	1741
5	1965	1855	1778
6	2000	1890	1814
7	2035	1926	1850

258 mbsf (BSR0)

S_H (%)	φ 40	φ 50	φ 60
0	1782	1671	1592
1	1819	1709	1630
2	1856	1746	1667
3	1893	1782	1704
4	1929	1819	1741
5	1965	1855	1778
6	2000	1890	1814
7	2035	1926	1850

360 mbsf (central basin)

S_H (%)	φ 40	φ 50	φ 60
0	1813	1699	1617
1	1850	1736	1654
2	1886	1772	1690
3	1922	1808	1727
4	1957	1844	1763
5	1992	1879	1799
6	2027	1914	1835
7	2062	1949	1871
8	2096	1984	1906

360 mbsf (BSR1)

S_H (%)	φ 40	φ 50	φ 60
0	1813	1699	1617
1	1850	1736	1654
2	1886	1772	1690
3	1922	1808	1727
4	1957	1844	1763
5	1992	1879	1799
6	2027	1914	1835
7	2062	1949	1871
8	2096	1984	1906

438 mbsf (central basin)

S_H (%)	φ 30	φ 40	φ 50	φ 60
0	2037	1832	1717	1632
1	2073	1869	1753	1669
2	2107	1904	1789	1705
3	2142	1940	1824	1742
4	2175	1975	1860	1777
5	2209	2009	1895	1813
6	2242	2044	1930	1849
7	2274	2078	1964	1884
8	2306	2112	1998	1919
9	2338	2145	2032	1954

438 mbsf (BSR3)

S_G (%)	φ 30	φ 40	φ 50	φ 60
0	2037	1832	1717	1632
1	1769	1561	1447	1361
2	1730	1522	1409	1323
3	1713	1505	1393	1307
4	1702	1494	1383	1297
5	1695	1486	1376	1290
6	1669	1462	1354	1270
7	1650	1444	1338	1257
8	1631	1427	1323	1244
9	1613	1410	1309	1231

Note that we do refer to V_P trends rather than to V_{INT} aiming to constrain physical parameters and their variability within layers, rather than identifying a single value of i.e., gas/gas hydrate saturation within layers based on V_{INT}. The other physical parameters used in the modelling (i.e., salinity, porosity, etc.) come from literature and we have no constraint on how they may vary within depth within a layer, so we assumed averaged values.

For each BSR depth and corresponding sub-seafloor depth in the central basin, we calculated the V_P assuming variable porosity of the sediment and variable amount of pore-floating hydrate (S_H) or gas-bearing (S_G) sediment. Results of these calculations are summarised in Fig. 12 and Table 3.

Modelling results show that the V_P ranges observed in the central basin may be explained by the assumed shale-dominated lithology, with a porosity decreasing from 60% to 40% from 258 m to 438 m depth bsf. These values are within ranges provided by recent studies that have reported a porosity of approximately 60% for the shallow sediments of the Black Sea, decreasing down to 50% at sediments around 150 mbsf (e. g., Vassilev, 2006; Riboulot et al., 2018; Merey, 2017). Thus, we consider 50% sediment porosity to be representative for the shallow sediments up to BSR1 depths. Sediment porosity might reduce with depth more rapidly in folded sediments (Fruehn et al., 1997), however, since no constraints are available on sediment porosity within the Tuapse Trough folded structures, we only refer to values from previous studies and estimates. Lower porosities ~30% may be assumed at greater depths (~600 mbsf).

Assuming porosities of around 50% in shallow sediments (up to BSR1 depths) in the central basin, the calculated V_P can match the observed velocity range simply assuming water saturated sediments (S_w of 100%). For the same 50% porosity, a pore-floating gas hydrate saturation of less than 2% and of 4 ± 2% needs to be considered above BSR0 and BSR1, respectively, to explain the observed velocities (Fig. 12a, b; Table 3). Thus, a higher amount of hydrate may be expected within the 100 m-thick layer between BSR0 and BSR1. The low-velocity zone imaged above BSR3 seems to be best described by a S_G of about 20–25%, for porosities between 30 and 40% (Fig. 12d; Table 3). Based on previous studies, a 30% porosity value is considered more representative for BSR3 stratigraphic depth. The V_P response at the deeper stratigraphic depth of ~600 mbsf was also modelled as a final test. This depth corresponds to an average observed V_P of about 2020 m/s for both the central basin and BSRs area (Fig. 9), and the calculated V_P matches the observed velocity assuming a fully water-saturated sediment with a porosity of 30%, which is in good agreement with the porosity and lithology expected at that depth. This confirms the absence of anomalous velocities that may be associated with hydrate or gas in the pore space at that depth.

6. Discussion

We observed multiple BSRs-like reflection within the Tuapse Trough, in the EBSB, which appear as linear but discontinuous seismic reflections, sub-parallel to the seafloor, crosscutting the background stratigraphy, and showing different seismic polarity (Fig. 3). Besides looking at the character of their seismic response, we investigated the physical properties of sediments at the multiple BSRs to provide an explanation for these reflections to be visible at the crest of a folded structure.

The first question arising when observing these multiple BSR-like reflections, is whether they can be considered hydrate-related reflectors or if they result from other factors not necessarily linked to the presence of gas hydrates, but which may also produce BSR-like reflections (see section 1). For instance, Berndt et al. (2004) have proved seismic reflections crosscutting the background sedimentary layers to be related to diagenetic boundaries rather than to the presence of a gas hydrate system. These types of BSR reflections are associated with the opal-C/opal-AT transition or the smectite/illite conversion which, like the hydrate phase boundary, are also pressure- and temperature

(P-T)-dependent and therefore mimic the seafloor. However, such diagenetic BSR reflections do not show opposite polarities with respect to the seafloor, and they generally form at greater depths since they require much higher temperatures (35–50 °C) to form. Our observed multiple BSR reflections show predominantly reversed polarity compared to the seafloor (Fig. 3), suggesting a signal response resulting from the presence of gas (or a slower layer) underneath the BSR; furthermore, they occur at relatively shallow depths where the temperature of the sub-seafloor sediments is expected to be less than 25 °C (Fig. 11B). As pointed out by previous studies, hydrate-related BSRs are generally visible at shallower stratigraphic depths compared to diagenetic BSRs as they are not stable at sediment's temperatures above 25 °C (Berndt et al., 2004; Mosher, 2011). For the above reasons, we exclude the hypothesis that our multiple BSRs may be associated with diagenetic boundaries.

Other mechanisms, such as the presence of different hydrate-forming gases or the presence of overpressure compartments may also explain multiple BSR reflections. The presence of different hydrate-forming gases changes the hydrate stability P-T conditions, and this effect may generate multiple BSRs (Andreassen et al., 2000; Geletti and Busetti, 2011). However, there is little evidence for the presence of relevant quantities of hydrate-forming gases other than methane in the Black Sea (e.g., Vassilev and Dimitrov, 2002; Poort et al., 2005; Zander et al., 2020). Also, although fractionation of thermogenic gas has been suggested to cause multiple BSRs, there is no evidence at any locations globally where this process has been confirmed (Han et al., 2021).

Overpressure compartments may also be present in sub-seafloor sediments, whose top and base may be imaged by seismic data as BSR-like reflections (e.g., Tinivella and Giustiniani, 2013). Gas-induced overpressure compartments may lead to low-frequency events in seismic data, since high-frequency components of the seismic energy are absorbed by gas (e.g., Geletti and Busetti, 2011). However, our seismic data do not show evident blanking effects or anomalous seismic velocities that may be associated with the presence of high amounts of gas. Furthermore, previous calculations from the WBSB where multiple BSRs have similar spacing in depth between them as the ones observed in this study, have shown that the presence of overpressure compartments can be excluded because the necessary gas column would exceed the vertical distance between two overlying BSRs (Zander et al., 2017). We therefore exclude that multiple BSRs identified in this study result from either change in gas composition or from the presence of overpressure compartments.

Excluding the above mechanisms for the observed multiple BSRs, we explore the gas hydrate-related explanation as it seems to best explain (i) seismic polarities at the observed BSRs, (ii) results of our travel-time analysis showing anomalous velocities compared to the reference values in the central basin, and (iii) rock physics modelling results. Below we review and discuss the physical properties derived from sediments at multiple BSRs (section 6.1), how we interpret the four BSRs in this study (section 6.2), and the possible mechanisms responsible for BSRs being visible on seismic data (section 6.3).

6.1. Physical properties of the multiple BSRs

Discontinuous BSRs, like the ones observed in our study area, are often associated with dipping sedimentary layers (interbedded sand and mud successions) with high-amplitude seismic facies generally truncated at the BGHSZ, resulting in the BSR reflection. While a BSR alone is typically considered an unreliable indicator for the presence of gas hydrates, a phase reversal along a single horizon that crosscuts the BSR may be a more robust indicator (Boswell et al., 2012; Portnov et al., 2021). High-amplitude reflectors below a BSR are generally associated with free gas accumulation, whereas high-amplitude and reversed-polarity reflections above BSRs are generally considered to result from enrichment of gas hydrate (Liu et al., 2021). At the EBSB multiple BSRs, we identified one phase reversal along a dipping seismic

reflector crosscutting BSR1, which may be indicative of gas hydrate saturation above this BSR (Fig. 3D). The same BSR1 seems to match the predicted BGHSZ assuming geothermal gradient values within ranges expected in this area (Fig. 11). Results from travel-time analysis, using both non-downward and downward continued reflected and refracted arrivals, have shown a V_P increase from seafloor down to BSR1, with BSR0 visible as a positive polarity reflector indicating a further increase in velocity gradient in sediments beneath (Fig. 3). V_P from seafloor to BSR0 (1.55–1.72 km/s) and from BSR0 to BSR1 (1.75–1.83 km/s) are higher than the V_P in the central basin from seafloor down to BSR0 (1.55–1.64 km/s) and from BSR0 down to a similar depth to BSR1 (1.64–1.72 km/s), which matches trends for a shale-dominated lithology expected in this area (Fig. 10). Seismic BSRs may be present in the central basin, although poorly imaged by the seismic data and masked by the sub-horizontal seafloor-parallel stratigraphy; however, there is no evidence for a low-velocity zone in the central basin sediments suggesting gas accumulation beneath the present-day BGHSZ (Fig. 11A). Furthermore, seismic velocities observed in the central basin can be explained by normal compaction of water-saturated shaley sediments and do not require the presence of gas hydrate, whereas seismic velocities at the multiple BSRs may indicate the presence of an S_H less than 2% from seafloor to BSR0 and of about $4 \pm 2\%$ from BSR0 to BSR1 (Fig. 12a, b). To note that we have assumed 50% porosity (e.g., Vassilev, 2006; Riboulot et al., 2018; Merey, 2017) and a pore invasive hydrate habit, which is generally associated to coarse-grained sediments, but the host sediment in the study area is expected to be a shale dominated lithology for which a particle displacing habit might be expected (e.g., Ren et al., 2020). Though, the assumed pore-floating habit and calculated hydrate saturations agree with observations from fine-grained muddy sediments

in systems with modest gas supply, indicating values below 10% and hydrate disseminated in the pore space (i.e., pore-floating, e.g., Holland et al., 2008; Boswell et al., 2012; Collett et al., 2014). As we do not have constraints on the hydrate habit at the study area, the calculated hydrate saturations that explain the observed high V_P should be taken with caution. Furthermore, although the higher velocities above BSR1 may alternatively be explained by tectonic compaction in the folded sediments, the abrupt increase in velocities below BSR0 is less readily explained by this mechanism.

Beneath the reversed polarity BSR1, a 70-80 m-thick layer including BSR2 and down to BSR3 was modelled, showing a seismic velocity decrease of approximately 12% (from 1.83 to 1.61–1.62 km/s). Such velocity decrease matches with the phase reversal observed along the dipping reflector cross-cutting BSR1 (Fig. 3D) and can be explained by a S_G of up to 25% (Fig. 12d) assuming a sediment porosity of 30% (i.e., Vassilev, 2006; Riboulot et al., 2018; Merey, 2017). This velocity trend and inferred saturations are not observed in sediments at similar sub-seafloor depths ($\sim$438 mbsf) in the central basin, where sediment's velocities match what expected for water-saturated sediments assuming normal compaction (Fig. 12c). The base for this free-gas zone seems to correspond with BSR3 reflection, beneath which seismic velocities increase again. However, we note that the seismic polarity at BSR3 reflector changes from a reversed polarity (west) to a normal polarity (east) (Fig. 3). This mismatch between the seismic response at BSR3 and the model can be explained if (i) the waveform of BSR3 is more complex than that of the other BSRs likely reflecting the interference with reflections from background sedimentary strata, or (ii) small velocity variations are present associated with thin layers immediately below BSR3, but these are not well represented by the thick layers of our
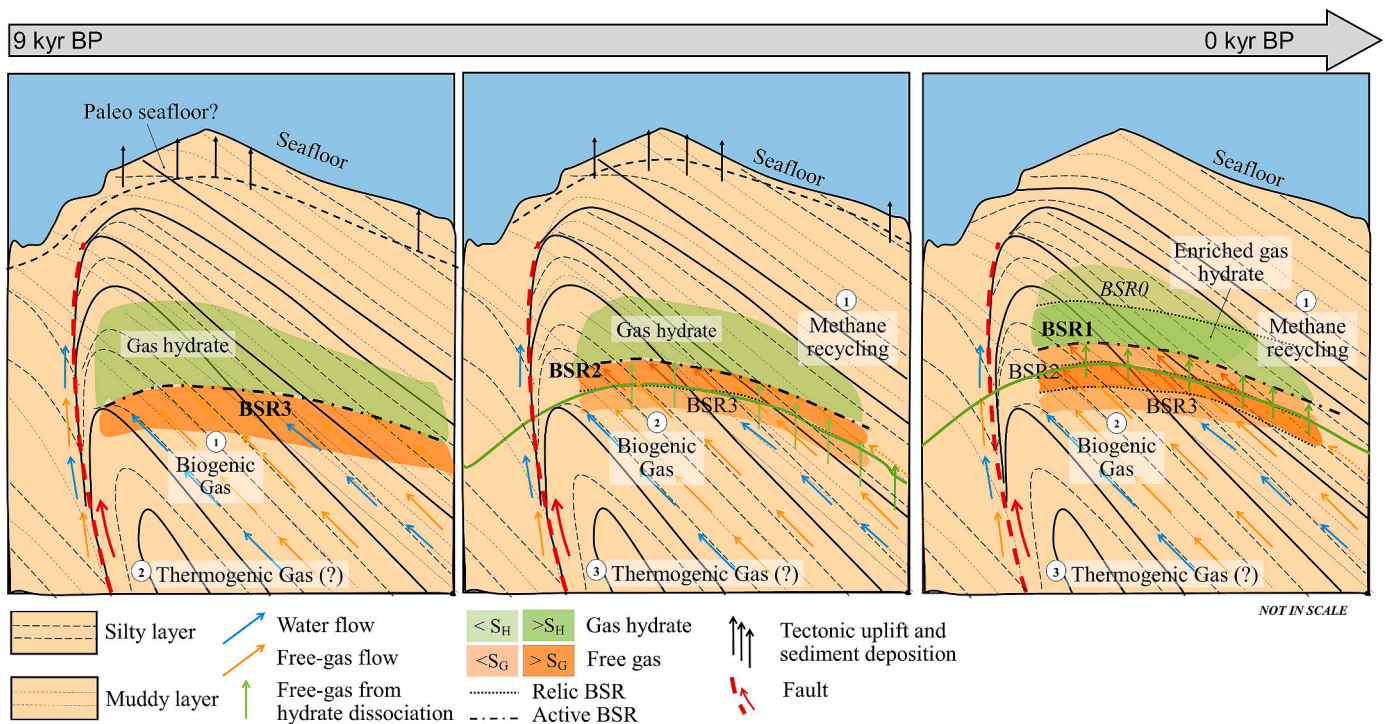

Fig. 13. Schematic diagrams showing the interpretation of the multiple BSRs, and the most likely formation mechanisms in the EBSB: (1) methane recycling and (2)–(3) free gas flow from beneath the BGHSZ, which may include microbial gas generated from beneath the BGHSZ and/or (2) thermogenic gas coming from deeper sources (3). Permeable pathways, such as folded stratigraphy and thrust fault(s), favour a focused fluid flow, accumulation and gas hydrate formation at the crest structure. BSR3 is interpreted as the oldest BSR. P-T changes (following the LGM) have progressively shifted the BGHSZ upwards leaving behind relict BSRs (BSR3 and BSR2), which are still visible on seismic data due to free gas being trapped in the pore space following the upward shift of the BGHSZ. BSR1 is interpreted as the present-day BGHSZ, and BSR0 is interpreted as the boundary between a lower gas hydrate concentration above (light green) and a higher gas hydrate concentration beneath (dark green), or possibly as the top of the GHOZ. Note that the lateral extent of free gas and gas hydrate accumulations reflects the lateral uncertainty in the velocity model. Free gas flow from layers deeper than the GHSZ cannot be excluded. Also, permeable pathways as dipping sedimentary layers and faults are considered to have favoured the formation of a localised gas hydrate accumulation. Diagram modified from You et al. (2019).

velocity model.

6.2. Interpretation of the EBSB multiple BSRs

Based on the seismic character, the inferred physical properties of sediments in the BSR area, and the results of our BGHSZ modelling, we interpret BSR1 to represent the present-day BGHSZ corresponding to a geothermal gradient of 26–30 °C/km (Figs. 11 and 13). Although these geothermal gradient values lie within ranges calculated/measured at other locations in the EBSB (e.g., Vassilev and Dimitrov, 2002; Minshull and Keddie, 2010) they are slightly lower than those observed at DSDP Hole 379A (32–38°C/km; Erickson and Von Herzen, 1978). Nevertheless, constraints on the local geothermal gradient are limited and often show high degree of variability (Vassilev, 2006), with localised tectonic deformation playing a significant role in controlling fluid and heat-flow (Riedel et al., 2021).

Above BSR1, BSR0 appears to be the acoustic boundary between lower (at the top) and higher (at the bottom) gas hydrate saturation within the hydrate stability zone; thus, we interpret BSR0 as the boundary between different amount of S_H, or as the top of the gas hydrate occurrence zone (GHOZ; Wood and Ruppel, 2000; Riedel and Collett, 2017; Boswell et al., 2016; Taladay et al., 2017) (Fig. 13). A dipping stratigraphic layer crosscutts BSR0, BSR1 and deeper layers, showing a higher amplitude and normal polarity character between BSR0 and BSR1, but not above BSR0 (Fig. 3); this same layer shows phase reversal underneath BSR1 (Fig. 3D). Amplitude-enhanced layers have previously been used to identify the extent of the GHOZ (e.g., Gulf of Mexico, Portnov et al., 2022; Makran Accretionary Prism; Liao et al., 2022). Log data from a hole drilled at a BSR site in the Gulf of Mexico has also demonstrated the relationship between such high amplitude, seafloor-like polarity reflections (also called enhanced-amplitude reflections) above a BSR with the presence of high gas hydrate saturations (Collett et al., 2012). Therefore, we interpret the higher amplitude of this dipping reflector to correspond to the higher gas hydrate saturation modelled between BSR0 and BSR1. Although we can only see one example of these enhanced-amplitude reflections (Fig. 3D), the lack of other enhanced-amplitude reflectors may be related to the small particle size of surface sediments (including silty-clay) and the low hydrate saturation with disseminated distribution (e.g., Bohrmann and Ohling, 2008). Nevertheless, seismic evidence seems to support the interpretation of BSR1 as the BGHSZ and of BSR0 as the top of the GHOZ.

Although BSR0 does not really represent a BSR based on our interpretation (it does not represent the present-day or past BGHSZs), we have labelled it as a BSR because it crosscuts stratigraphy and is sub-parallel to the seabed; the top of the GHOZ would also be expected to cross-cut stratigraphy, but any geometrical relationship to the seabed would probably be coincidental. BSR-like reflections associated with the top of the GHOZ are rarely observed (e.g., South China Sea; Wang et al., 2018). This absence of reflection has been explained in different ways: (i) the gas hydrate concentrations decrease gradually towards the seafloor (Andreassen et al., 1997), (ii) the limited resolution of seismic data preventing proper imaging (Hyndman and Spence, 1992) or (iii) the presence of disseminated gas hydrate present as small-scale nodules that has limited impact on seismic velocity (Nasif et al., 2020). Point (iii) has been used to explain the absence of a visible top of the GHOZ in the south-western Black Sea, based on evidence from sampled gas hydrates offshore Crimea, Georgia and Sorokin Trough which showed the presence of small gas hydrate crystals or finely disseminated gas hydrates dispersed in the mud within the uppermost sediments (Limonov et al., 1997; Woodside et al., 2003; Bohrmann et al., 2003; Klaucke et al., 2006; Sahling et al., 2009). Therefore, our study may be providing the first evidence for the top of the GHOZ in the Black Sea region.

Below BSR1, BSR2 lies within a low-velocity zone which base is represented by BSR3. We interpret BSR2 and BSR3 to represent relict BSRs marking a previous BGHSZ that shifted upwards following a perturbation of the gas hydrate stability field. The reason for the ongoing

visibility of BSR2 and BSR3 reflections may be the presence of free gas liberated from hydrate dissociation that has been left behind (trapped) within the pore space of sediments (Fig. 13). Following dissociation of pore floating hydrate, which is a non-load bearing, the liberated pore space is then occupied by water and gas with no mechanical compaction occurring. Assuming that the rate of pressure dissipation is smaller than of hydrate dissociation (low permeability), the porosity increases because metastable solid hydrate is replaced by fluids. As porosity increases due to hydrate dissociation with no mechanical compaction, V_P decreases (Fig. 12B) because the V_P of hydrate is larger than those of water and methane. During hydrate dissociation, a small fraction of the released gas can be trapped in the smaller pores, also contributing to a decrease in V_P. These mechanisms can explain the negative polarity of BSR2 and BSR3, which are therefore still visible as associated with the presence of relict gas (Fig. 13).

6.3. Potential origins of multiple BSRs

6.3.1. Methane recycling

Our results and interpretation of the multiple BSRs favour an upward shift of the gas hydrate stability field in the EBSB, which may be explained through a methane recycling mechanism (Fig. 13). Hydrate-sourced methane recycling is one of the most common mechanisms proposed at multiple BSRs locations, including BSRs from the Danube Fan in the WBSB (e.g., Kvenvolden, 1993; Pecher et al., 1996; Haacke et al., 2007), and it occurs when gas hydrate dissociates, migrates and reforms within new stability conditions. Gas hydrate dissociation is controlled by changes in the system's P-T following increased sedimentation rates, subsidence, increased temperatures due to climatic changes, heat flow variations, and/or tectonic uplift. The free gas generated upon dissociation flows upwards and may reform hydrate immediately above the BGHSZ, although some of the free gas may be left behind within the sediment's pore space (e.g., Marín-Moreno et al., 2015; You et al., 2019). Thus, methane recycling can explain the presence of higher hydrate concentrations at the BGHSZ and the free gas beneath it (e.g., Blake Ridge, Flemings et al., 2003; South China Sea, Wang et al., 2014). Multiple BSRs in the EBSB are therefore interpreted as resulting from dissociation, indicating the presence of dynamic hydrate systems and recording both the shifted modern and relic base(s) of the GHSZ (Fig. 13).

Variations in the P-T system following sea-level and bottom water temperatures changes due to glacial cycles have been proposed to explain multiple BSR formation in some regions, including the WBSB (Bangs et al., 2005; Popescu et al., 2006). Rising sea-level during deglaciation is usually accompanied by bottom water temperature warming, while the opposite occurs during glaciation (Ruppel and Kessler, 2017; Screaton et al., 2019). Thus, changes of sea-level and bottom water temperature have opposing effects on BGHSZ depth. Studies from the WBSB have shown that multiple BSRs in that part of the basin can be related to methane recycling mechanisms driven by variations in the paleo-environmental conditions of the Black Sea during the Quaternary; these conditions have been derived from the Danube Fan area and are supported by information from litho-facies analysis from DSDP Sites 380 and 381 (Fig. 1). Since the LGM, the paleo-environmental conditions of the Black Sea resembled that of a lake in which marine ingress caused an eustatic sea-level rise of 100–150 m (e.g., Popescu et al., 2006, 2007; Zander et al., 2017; Ker et al., 2019; Vassilev, 2006; Ryan et al., 2003) and a seafloor temperature increase of 4–5 °C (e.g., Soulet et al., 2010). Sea-level rise would generate a pressure increase, and thus cause a downward shift of the BGHSZ, whereas a seafloor temperature increase would cause an upward shift of the BGHSZ. Typically, the hydrate system should respond more rapidly to pressure field changes in the subsurface, while temperature changes might require more time to reach the BGHSZ (Foucher et al., 2002; Pecher et al., 2017; Zander et al., 2017). However, Poort et al. (2005) argued that the pressure changes due to the increase in sea-level

following the end of the LGM were slowly counteracted by a simultaneous increase in bottom water temperature from 4-5 °C to 9 °C. Therefore, lower values in today's near-seabed geothermal gradient have been interpreted to be still influenced by the increase of the bottom water temperature since the LGM, suggesting that thermal system in the Danube fan still adapts to this change and is not in steady state (Riedel et al., 2021). As a result, the BGHSZ is expected to become shallower over the next tens of thousands of years as the geotherm increases due to thermal diffusion (Poort et al., 2005; Zander et al., 2017).

If we assume a sea-bottom temperature increase, we expect an upward shift of the BGHSZ explaining the present-day stability field which seems to be associated primarily to BSR1 rather than with the deeper BSRs. This post-glacial evolution is similar to what observed in the WBSB, where the BGHSZ has also migrated upwards following changes in the temperature field (Zander et al., 2017). However, enhanced sediment loading due to rapid deposition in the Danube Fan area has also been considered a major element that controlled heat conduction from below the BGHSZ and the pressure field in sediments, thus affecting the hydrate system and contributing to the formation of multiple BSR (Zander et al., 2017). Zander et al. (2017) noted that the sediment load above the multiple BSRs grew during the past glacial cycles and was not constant as assumed by other studies (i.e., Popescu et al., 2006), thus leading to large errors when the BSRs are linked to ranges of lower bottom-water temperatures during stable cold climate periods. Based on this evidence, Zander et al. (2017) invoked increased sedimentation rates as a key factor for methane recycling processes in the WBSB.

Although sedimentation processes have also being ongoing in the EBSB, their effects may have been counteracted by tectonic uplift as our study area has also experience compressional deformation (fold-and-trust belt development) since the Oligocene. Thus, the EBSB shows different tectono-stratigraphic settings compared to the nearby the WBSB where multiple BSRs have been studied; the WBSB multiple BSRs lie in an area of the basin where the high sedimentation rates of the Danube Fan are predominant (e.g., Zander et al., 2017). All other BSRs identified in the EBSB, where the compressional regime and the tectono-stratigraphic settings may resemble better the ones in the Tuapse Trough, were single BSRs only (e.g., Minshull and Keddie, 2010). Thus, multiple BSRs in the compressional settings of the Tuapse Trough fold-and-thrust belt are unique and not directly comparable to other gas hydrate related multiple BSRs systems in the Black Sea. Compressional forces at the Tuapse Trough areas would have resulted in tectonic uplift, followed by a reduction in hydrostatic pressure of the sediments and consequent upward shift of the BGHSZ (Goto et al., 2016). Erosion on top of the uplifted anticline structure could lead to a downward movement of the BGHSZ, whereas increased heat flow, e.g., conductive heat flow on the flanks of the folded structure, would lead to an upward shift (Crutchley et al., 2011). Our evidence suggests an upward shift of the BGHSZ; thus, tectonic uplift and/or conductive heat flow may have had a role in the methane recycling processes in the EBSB, together with the temperature increase and/or an increase in sedimentation rates controlling heat conduction in sediments. Although our results show that multiple BSR generation in the EBSB may have closer similarity with the dynamics occurring at depositional and compressional settings (i.e., offshore Panama, Reed et al., 1990; Hikurangi Margin, Pecher et al., 2005; Crutchley et al., 2019), a better knowledge of the tectonic uplift rates, sedimentation rates, and heat conduction in sediments of the Tuapse Trough would be required to properly assess each factor's contribution to the evolution of the BGHSZ in this part of the EBSB.

Assuming an upward shift of the BGHSZ, BSR3 and BSR2 represent relics of past gas hydrate stability conditions which are interpreted to be still visible because of the presence of trapped gas in the pore space. Other studies have invoked the possibility that relict BSRs are still visible because of their lithification following a long period of hydrate stability (e.g., Popescu et al., 2006). However, BSR3 and BSR2 reversed seismic polarities and results from travel-time analysis seems to suggest they are

most probably related to the presence of relict gas generating the visible acoustic impedance contrasts. While the gas hydrate stability field has migrated upwards, some gas may have been trapped in the previous GHSZ. Given the negative polarity of BSR2, which lies within the 70-80 m-thick low-velocity zone, we may infer that a higher free gas saturation is present in the layer between BSR2 and BSR3, compared to the layer between BSR1 and BSR2 (Fig. 13). Another interpretation may be that BSR3 represents the base of a free gas zone formed by a deeper gas supply, while BSR2, sitting within the free gas zone, could effectively represent a paleo-BSR. Results from a recent study investigating paleo-BSRs along the Central-South Chilean margin have shown that, although free gas presence can be related to gas hydrate dissociation due to climate change and geological evolution, if the base of the free gas is deeper than the paleo-BSR thus resulting in a thicker free gas zone, a deeper gas supply can be invoked (Vargas-Cordero et al., 2021).

The tectonic settings encountered at the EBSB multiple BSRs would have favoured a greater and focused amount of fluid supply to the crest structure where BSRs are observed, which may explain the inferred gas hydrate and free gas distribution and saturation. Although our velocity model may be limited in constraining the lateral extent of the physical changes at the BSRs, these changes appear to be focused exactly at the crest of the folded structure where multiple BSRs are imaged, thus supporting the idea of focused fluid flow (Figs. 9 and 10). The presence of single and multiple BSRs at anticline structures has been reported at other sites (e.g., Makran accretionary prism), where fluid migration pathways including deep faults, gas chimneys, and high-permeability layers play an important role in controlling hydrate and gas migration and distribution (Liu et al., 2021). A low-velocity zone of a few meters to many tens of meters thick caused by the presence of gas at low saturation is commonly observed below the BGHSZ (e.g., Singh et al., 1993; MacKay et al., 1994; Hovland et al., 1997). Besides the gas released by hydrate dissociation which may still be in a transient state or trapped and has not migrated upward into the new GHSZ (e.g., Zander et al., 2017), the tectonic settings at the EBSB multiple BSRs indicate that the free gas zone beneath BSR1 may also have other contributing origins related to: (i) deeply sourced fluids that have migrated upwards along folded sediments or along fractures/faults (e.g., Crutchley et al., 2019), (ii) in-situ biogenic gas generation (e.g., Schneider et al., 2016), or (iii) a combination of these origins, including gas formed by hydrate dissociation, deeply sourced fluids, and in-situ biogenic gas (Fig. 13).

6.3.2. Upward migration of deeply sourced fluids

The presence of potentially deep faults associated with folding and thrusting in the Tuapse Trough, together with the dipping geometries of the stratigraphic layers alternating fine- and coarse-grained material (Fig. 2), provide plausible pathways for the focused migration and accumulation of gas at the crest of the anticline structure where multiple BSRs are observed (Fig. 13). When free gas flow takes place along permeable pathways, such as permeable or fractured fault systems or coarse-grained sediment layers (Collett et al., 2009; Nole et al., 2016), it may focus toward topographic or structural highs by buoyancy (e.g., crests of ridges or anticlines; Flemings et al., 2003; Frederick and Buffett, 2011; Boswell et al., 2012). Such permeable pathways are commonly observed in concentrated gas hydrate accumulations (e.g., Crutchley et al., 2019). Bedding-parallel fluid flow at anticlinal ridges and fluid upward migration along thrust faults have also been inferred at a few other gas hydrate locations, i.e., offshore Taiwan (Lin et al., 2008), Hikurangi Margin offshore New Zealand (Crutchley et al., 2019; Han et al., 2021), Nankai Margin (Ashi et al., 2002).

Free gas fluid flow from beneath the BGHSZ would explain the higher hydrate saturation between BSR0 and BSR1. Previous studies have shown that local free gas flow often results in high hydrate saturation values up to or more than 90% for sand-dominated sediments (e.g., You and Flemings, 2018). Our results point towards gas hydrate saturations of less than 6% at BSR1, thus showing lower saturation values than other studies. Numerous mud volcanoes and seeps related to fluid expulsion

have been reported in this same area (e.g., Vassilev and Dimitrov, 2002; Meisner et al., 2009), which may indicate that some gas has escaped through the sedimentary layers up to seabed and water column; however, no evidence for fluid expulsion (i.e., pipes, chimneys) or clear faults/fractures through the GHSZ are visible on our seismic profile. Gas hydrate may exist in clay-rich sediments within the faults and fractures reaching quite high saturations; however, gas hydrate may still show up with extremely low saturations if fracture density is low (e.g., Waite et al., 2019), thus possibly explaining both why the BSRs are only seen within the folded sediments of the Tuapse Trough, and the low saturation observed. Based on the considerations above, localized fluid flow may represent one of the mechanisms driving free gas accumulation beneath BSR1 and gas hydrate formation just above BSR1. Similar stratigraphic/structural control over the hydrate system has been inferred from multiple BSRs in the WBSB, although control elements are linked to the channel-levee depositional settings encountered in that area (Popescu et al., 2006; Han et al., 2021; Riedel et al., 2021).

6.3.3. In-situ biogenic gas generation

Another possible source of gas may be microbial biogenesis of organic-rich material buried beneath the BGHSZ (e.g., Schneider et al., 2016). Given the high organic content characterising the Miocene, Pliocene, and Quaternary units of the EBSB (Tari and Simmons, 2018), it is possible that free gas beneath BSR1 could derive from biogenic gas. Low methane hydrate saturations, in the range of 1–10% (e.g., Malinverno, 2010) would result from biogenic gas contributing to hydrate formation at the BGHSZ. Given the localised nature of the free gas accumulation between BSR1 and BSR3, this free gas may have migrated laterally through permeable pathways focusing on the anticlinal structure beneath BSR1 (Fig. 13).

In summary, our results suggests that multiple BSRs in the EBSB are related to mechanisms of methane recycling following hydrate dissociation. Hydrate dissociation would have been caused by temperature changes due to climatic changes, and possibly also due to tectonic uplift, and/or erosion and sedimentation processes (Fig. 13). The release of free gas from hydrate dissociation would have migrated upward again into the GHSZ to re-form hydrate. Within this system, the contribution of microbial biogenesis and upward migration of deeper fluids beneath the BGHSZ cannot be excluded.

7. Conclusions

A long-offset seismic reflection profile reveals, for the first time, evidence for multiple BSR reflections along the compressional NE margin of the EBSB. This profile was used to extract the V_P structure and gas and hydrate saturations, thus constraining the nature of the observed BSRs and the mechanisms for their presence.

Downward continuation was used to pre-condition seismic data before reflection and refraction travel-time analysis, resulting in improved first arrival refractions. Nevertheless, refracted events still come from layers deeper than the observed BSRs, and artefacts and noise at near offsets limit first arrival refraction picking. The close spacing between the BSR layers, the presence of a low-velocity zone, and the geological complexity of the area, pose limitations for the downward continuation technique and for picking of first arrivals related to the BSRs. Thus, the velocity model also strongly relies on reflected travel-time information from non-downward-continued data.

Combined travel-time analysis and effective-medium modelling show that the two topmost BSRs, BSR0 and BSR1, are associated with less than 2% and about $4 \pm 2\%$ pore-floating gas hydrate saturation respectively, assuming a 50% sediment porosity. Based on these estimates, we infer that BSR0 (at 258 mbsf) may represent the top of the GHOZ, or the acoustic boundary between sediments showing different amounts of hydrate saturation, whereas BSR1 (at 360 mbsf) represents the base of enriched hydrate accumulation directly above the BGHSZ. The depth of BSR1 shows good agreement with the depth of the

modelled BGHSZ for a geothermal gradient between 26 and 30 °C/km, consistent with heat-flow estimates in the EBSB. Beneath BSR1, a 70-80m-thick low-velocity zone with $25 \pm 10\%$ free gas saturation includes BSR2 (at 395 mbsf) and extends down to the depth of BSR3 (at 438 mbsf).

We infer that the higher gas hydrate concentration above BSR1, and evidence for free gas beneath BSR1, may be explained by mechanisms of methane recycling following primarily temperature driven gas hydrate dissociation. The contribution from biogenic (and/or thermogenic) free gas flow from beneath the BGHSZ cannot be excluded. Differential erosion/deposition at the crest structure and uplift may have also played an important role in altering the sediments pressure field causing an upward shift in the BGHSZ, although further information is needed to assess their contribution to methane recycling processes.

The deeper BSRs are interpreted as relics of past hydrate stability conditions, defining the base of the gas layer (BSR3) and an intermediate level of the BGHSZ upward shift (BSR2). The fact that these deeper BSRs are still visible on seismic data is attributed to the presence of free gas being trapped following the upward shift of the BGHSZ. The localised nature of the hydrate and free gas accumulations are linked to the tectono-stratigraphic setting of the area, resulting in a focused gas and hydrate accumulation at the crest of the folded structure where BSRs are visible.

Given the limited constraints on the model parameters, saturation estimates strongly depend on the assumed sediment composition, porosity, and hydrate habit. For a more robust estimate of hydrate and gas saturation in our study area, further constraints on the physical and chemical properties of the sediments (i.e., borehole measurements) are needed. More and possibly densely spaced seismic profiles are necessary to better understand the interaction of the gas hydrate system with the tectonic setting and to constrain the presence and relevance of potential fluid migration pathways. Finally, to assess the impact of tectono-sedimentary processes on the gas hydrate system in this part of the EBSB, a knowledge of rates of uplift and rates of sediment deposition is needed.

Petrel software that was used for seismic display, interpretation, and depth conversion. RAYINVR forward ray-tracing algorithm presented in Zelt and Smith (1992) was used in a layer-stripping approach. The open source QGIS software was used for bathymetric map and seismic profiles plotting, and MATLAB was used to calculate and plot the BGHSZ and results from the effective-medium modelling. The seafloor temperature data used in this study are from NOAA database and are available at https://www.nodc.noaa.gov/OC5/woa18f/. VM was supported by Natural Environment Research Council Centre for Doctoral Training in Oil and Gas (nerc-cdt-oil-and-gas.ac.uk).

Appendix A. Supplementary data

Supplementary data to this article can be found online at https://doi.org/10.1016/j.marpetgeo.2023.106604.

References

Adamia, S., Alania, V., Chabukiani, A., Chichua, G., Enukidze, O., Sadradze, N., 2010. Evolution of the late cenozoic basins of Georgia (SW Caucasus): a review. Geological Society, London, Special Publications 340 (1), 239–259.

Almendinger, O.A., Mityukov, A.V., Myasoedov, N.K., Nikishin, A.M., 2011. Modern erosion and sedimentation processes in the deep-water part of the Tuapse Trough based on the data of 3D seismic survey. In: Doklady Earth Sciences, vol. 439. SP MAIK Nauka/Interperiodica, pp. 899–901, 1.

Andreassen, K., Hart, P.E., MacKay, M., 1997. Amplitude versus offset modeling of the bottom simulating reflection associated with submarine gas hydrates. Marine Geology 137 (1–2), 25–40. https://doi.org/10.1016/S0025-3227(96)00076-X.

Andreassen, K., Mienert, J., Bryn, P., Singh, S.C., 2000. A double gas-hydrate related bottom simulating reflector at the Norwegian continental margin. Ann. N. Y. Acad. Sci. 912 (1), 126–135.

Arnulf, A.F., Harding, A.J., Kent, G.M., Singh, S.C., Crawford, W.C., 2014. Constraints on the shallow velocity structure of the Lucky Strike Volcano, Mid-Atlantic Ridge, from downward continued multichannel streamer data. J. Geophys. Res. Solid Earth 119 (2), 1119–1144.

Arnulf, A.F., Singh, S.C., Harding, A.J., Kent, G.M., Crawford, W., 2011. Strong seismic heterogeneity in layer 2A near hydrothermal vents at the Mid-Atlantic Ridge. Geophys. Res. Lett. 38 (13).

Ashi, J., Tokuyama, H., Taira, A., 2002. Distribution of methane hydrate BSRs and its implication for the prism growth in the Nankai Trough. Mar. Geol. 187 (1–2), 177–191. https://doi.org/10.1016/S0025-3227(02)00265-7.

Auguy, C., Calvès, G., Calderon, Y., Brusset, S., 2017. Seismic evidence of gas hydrates, multiple BSRs and fluid flow offshore Tumbes Basin, Peru. Mar. Geophys. Res. 38 (4), 409–423.

Bangs, N.L., Musgrave, R.J., Tréhu, A.M., 2005. Upward shifts in the southern Hydrate Ridge gas hydrate stability zone following postglacial warming, offshore Oregon. J. Geophys. Res. Solid Earth 110 (B3).

Berndt, C., Bünz, S., Clayton, T., Mienert, J., Saunders, M., 2004. Seismic character of bottom simulating reflectors: examples from the mid-Norwegian margin. Mar. Petrol. Geol. 21 (6), 723–733.

Berryhill, J.R., 1979. Wave-equation datuming. Geophysics 44 (8), 1329–1344.

Berryhill, J.R., 1984. Wave-equation datuming before stack. In: *SEG Technical Program Expanded Abstracts* 1984. Society of Exploration Geophysicists, pp. 397–399.

Best, A.I., Priest, J.A., Clayton, C.R.I., Rees, E.V.L., 2013. The effect of methane hydrate morphology and water saturation on seismic wave attenuation in sand under shallow sub-seafloor conditions. Earth Planet Sci. Lett. 368, 78–87. https://doi.org/10.1016/j.epsl.2013.02.033.

Bialas, J., Bohlen, T., Dannowski, A., Eisenberg-Klein, G., Gassner, L., Gehrmann, R., et al., 2020. Joint interpretation of geophysical field experiments in the danube deep-sea fan, Black Sea. Mar. Petrol. Geol. 121, 104551.

Biot, M.A., 1956. Theory of propagation of elastic waves in a fluid-saturated porous solid. II. Higher frequency range. J. Acoust. Soc. Am. 28 (2), 179–191. https://doi.org/10.1121/1.1908239.

Bohrmann, G., Ahrlich, F., Bachmann, K., Bergenthal, M., Beims, M., Betzler, C., et al., 2018. R/V METEOR cruise report M142, drilling gas hydrates in the danube deep-sea fan, Black Sea, varna–varna–varna, 04 november–22 november–09 december 2017. Berichte, MARUM–Zentrum für Marine Umweltwissenschaften, Fachbereich Geowissenschaften, Universität Bremen 320, 1–121.

Bohrmann, G., Ivanov, M., Foucher, J.P., Spiess, V., Bialas, J., Greinert, J., et al., 2003. Mud volcanoes and gas hydrates in the Black Sea: new data from Dvurechenskii and Odessa mud volcanoes. Geo Mar. Lett. 23, 239–249. https://doi.org/10.1007/s00367-003-0157-7.

Bohrmann, G., Ohling, G., 2008. Cold Seeps of the Makran Subduction Zone (Continental Margin of Pakistan): R/V Meteor Cruise Report M74/3:M74, Leg3, Fujairah-Male 30 October-28 November, 2007. Fachbereich Geowissenschaften, Universitat Bremen, pp. 1–120.

Boswell, R., Collett, T.S., Frye, M., Shedd, W., McConnell, D.R., Shelander, D., 2012. Subsurface gas hydrates in the northern Gulf of Mexico. Mar. Petrol. Geol. 34 (1), 4–30. https://doi.org/10.1016/j.marpetgeo.2011.10.003.

Boswell, R., Shipp, C., Reichel, T., Shelander, D., Saeki, T., Frye, M., et al., 2016. Prospecting for marine gas hydrate resources. Interpretation 4 (1), SA13–SA24.

Calvert, S.E., Batchelor, C.H., 1978. Major and minor element geochemistry of sediments from hole 379A, Leg 42B. Deep-Sea Drilling Project Initial Reports of the Deep Sea Drilling Project 42 (2), 527–541.

Chand, S., Minshull, T.A., Gei, D., Carcione, J.M., 2004. Elastic velocity models for gas-hydrate-bearing sediments—a comparison. Geophys. J. Int. 159 (2), 573–590.

Chazallon, B., Rodriguez, C.T., Ruffine, L., Carpentier, Y., Donval, J.P., Ker, S., Riboulot, V., 2021. Characterizing the variability of natural gas hydrate composition from a selected site of the Western Black Sea, off Romania. Mar. Petrol. Geol. 124, 104785.

Cifci, G., Ozel, S., Okay, S., Atgin, O., Ozel, O., Barin, B., et al., 2012. Eastern Black Sea gas hydrate related structures in eastern Black Sea. In: In EGU General Assembly Conference Abstracts, 10753.

Claerbout, J.F., 1976. Fundamentals of Geophysical Data Processing, vol. 274. McGraw-Hill, New York.

Collett, T.S., Boswell, R., Cochran, J.R., Kumar, P., Lall, M., Mazumdar, A., et al., 2014. Geologic implications of gas hydrates in the offshore of India: Results of the National Gas Hydrate Program Expedition 01. Marine and Petroleum Geology 58, 3–28. https://doi.org/10.1016/j.marpetgeo.2014.07.021.

Collett, T.S., Johnson, A., Knapp, C., Boswell, R., 2009. Natural gas hydrates: a review. In: Collett, T.S., Johnson, A., Knapp, C., Boswell, R. (Eds.), Natural Gas Hydrates—Energy Resource Potential and Associated Geologic Hazards, vol. 89. AAPG Memoir, pp. 146–219.

Collett, T.S., Lee, M.W., Zyrianova, M.V., Mrozewski, S.A., Guerin, G., Cook, A.E., Goldberg, D.S., 2012. Gulf of Mexico gas hydrate joint industry project Leg II logging-while-drilling data acquisition and analysis. Mar. Petrol. Geol. 34 (1), 41–61. https://doi.org/10.1016/j.marpetgeo.2011.08.003.

Cook, A.E., Tost, B.C., 2014. Geophysical signatures for low porosity can mimic natural gas hydrate: an example from Alaminos Canyon, Gulf of Mexico. J. Geophys. Res. Solid Earth 119 (10), 7458–7472. https://doi.org/10.1002/2014JB011342.

Crutchley, G.J., Gorman, A.R., Pecher, I.A., Toulmin, S., Henrys, S.A., 2011. Geological controls on focused fluid flow through the gas hydrate stability zone on the southern Hikurangi Margin of New Zealand, evidenced from multi-channel seismic data. Mar. Petrol. Geol. 28 (10), 1915–1931. https://doi.org/10.1016/j.marpetgeo.2010.12.005.

Crutchley, G.J., Kroeger, K.F., Pecher, I.A., Gorman, A.R., 2019. How tectonic folding influences gas hydrate formation: New Zealand's Hikurangi subduction margin. Geology 47 (1), 39–42. https://doi.org/10.1130/G45151.1.

Dai, S., Santamarina, J.C., Waite, W.F., Kneafsey, T.J., 2012. Hydrate morphology: physical properties of sands with patchy hydrate saturation. J. Geophys. Res. 117, B11205 https://doi.org/10.1029/2012JB009667.

Degens, E.T., Ross, D.A., 1974. Black Sea–Geology, Chemistry, and Biology.

Dickens, G.R., Quinby-Hunt, M.S., 1994. Methane hydrate stability in seawater. Geophys. Res. Lett. 21 (19), 2115–2118.

Dondurur, D., Çifçi, G., 2009. Anomalous strong reflections on high resolution seismic data from the Turkish Shelf of the Eastern Black Sea: possible indicators of shallow hydrogen sulphide-rich gas hydrate layers. Turk. J. Earth Sci. 18 (2), 299–313. https://doi.org/10.3906/yer-0801-1.

Dondurur, D., Küçük, H.M., Çifçi, G., 2013. Quaternary mass wasting on the western Black Sea margin, offshore of Amasra. Global Planet. Change 103, 248–260.

Ecker, C., Dvorkin, J., Nur, A.M., 2000. Estimating the amount of gas hydrate and free gas from marine seismic data, 10.1190/1.1444752.Edwards et al., 2009 Geophysics 65 (2), 565–573.

Ecker, C., Dvorkin, J., Nur, A., 1998. Sediments with gas hydrates: internal structure from seismic AVO. Geophysics 63 (5), 1659–1669. https://doi.org/10.1190/1.1444462.

Egorov, V., Artemov, Y.G., Gulin, S.B., Polikarpov, G.G., 2011. Methane seeps in the Black Sea: discovery, quantification and environmental assessment. J. Black Sea—Mediterranean Environ. (2), 171–185.

Erickson, S.N., Von Herzen, R.P., 1978. Downhole temperature measurements and heat flow data in the Black Sea—DSDP Leg 42B. Initial Rep. Deep Sea Drill. Proj. 42, 985–1103, 1975.

Flemings, P.B., Liu, X., Winters, W.J., 2003. Critical pressure and multiphase flow in Blake Ridge gas hydrates. Geology 31 (12), 1057–1060. https://doi.org/10.1130/G19863.1.

Frederick, J.M., Buffett, B.A., 2011. Topography- and fracture-driven fluid focusing in layered ocean sediments. Geophys. Res. Lett. 38, L08614 https://doi.org/10.1029/2010GL046027.

Fruehn, J., White, R.S., Minshull, T.A., 1997. Internal deformation and compaction of the Makran accretionary wedge. Terra. Nova 9 (3), 101–104. https://doi.org/10.1046/j.1365-3121.1997.d01-13.x.

Foucher, J.P., Nouzé, H., Henry, P., 2002. Observation and tentative interpretation of a double BSR on the Nankai slope. Mar. Geol. 187 (1–2), 161–175.

Gassner, L., Gerach, T., Hertweck, T., Bohlen, T., 2019. Seismic characterization of submarine gas-hydrate deposits in the Western Black Sea by acoustic full-waveform inversion of ocean-bottom seismic data. Geophysics 84 (5), B311–B324.

Gazdag, J., 1978. Wave equation migration with the phase-shift method. Geophysics 43 (7), 1342–1351.

GEBCO Compilation Group, 2019. GEBCO 2019 Grid. https://doi.org/10.5285/836f016a-33be-6ddc-e053-6c86abc0788e. (Accessed 14 October 2019). https://www.gebco.net/.

Geletti, R., Busetti, M., 2011. A double bottom simulating reflector in the western Ross Sea, Antarctica. J. Geophys. Res. Solid Earth 116 (B4).

Ginsburg, G.D., Soloviev, V.A., 1998. Methane migration within the submarine gas-hydrate stability zone under deep-water conditions. Mar. Geol. 137 (1–2), 49–57.

Goto, S., Matsubayashi, O., Nagakubo, S., 2016. Simulation of gas hydrate dissociation caused by repeated tectonic uplift events. J. Geophys. Res. Solid Earth 121 (5), 3200–3219. https://doi.org/10.1002/2015JB012711.

Haacke, R.R., Westbrook, G.K., Hyndman, R.D., 2007. Gas hydrate, fluid flow and free gas: formation of the bottom-simulating reflector. Earth Planet Sci. Lett. 261 (3–4), 407–420. https://doi.org/10.1016/j.epsl.2007.07.008.

Han, S., Bangs, N.L., Hornbach, M.J., Pecher, I.A., Tobin, H.J., Silver, E.A., 2021. The many double BSRs across the northern Hikurangi margin and their implications for subduction processes. Earth Planet Sci. Lett. 558, 116743 https://doi.org/10.1016/j.epsl.2021.116743.

Harding, A.J., Arnulf, A.F., Blackman, D.K., 2016. Velocity structure near IODP Hole U1309D, Atlantis Massif, from waveform inversion of streamer data and borehole measurements. G-cubed 17 (6), 1990–2014.

Harding, A.J., Kent, G.M., Blackman, D.K., Singh, S., Canales, J.P., 2007. A new method for MCS refraction data analysis of the uppermost section at a Mid-Atlantic Ridge core complex. AGU Fall Meeting Abstracts 2007. S12A-03.

Heeschen, K.U., Haeckel, M., Klaucke, I., Ivanov, M.K., Bohrmann, G., 2011. Quantifying in-situ gas hydrates at active seep sites in the eastern Black Sea using pressure coring technique. Biogeosciences 8 (12), 3555–3565. https://doi.org/10.5194/bg-8-3555-2011.

Helgerud, M.B., Waite, W.F., Kirby, S.H., Nur, A., 2009. Elastic wave speeds and moduli in polycrystalline ice Ih, sI methane hydrate, and sII methane-ethane hydrate. J. Geophys. Res. Solid Earth 114 (B2).

Henig, A.S., Blackman, D.K., Harding, A.J., Canales, J.P., Kent, G.M., 2012. Downward continued multichannel seismic refraction analysis of Atlantis Massif oceanic core complex, 30° N, Mid-Atlantic Ridge. G-cubed 13 (5).

Hillman, J.I.T., Burwicz, E., Zander, T., et al., 2018. Investigating a gas hydrate system in apparent disequilibrium in the Danube Fan, Black Sea. Earth Planet Sci. Lett. 502, 1–11. https://doi.org/10.1016/j.epsl.2018.08.051.

Hobro, J.W., Singh, S.C., Minshull, T.A., 2003. Three-dimensional tomographic inversion of combined reflection and refraction seismic traveltime data. Geophys. J. Int. 152 (1), 79–93. https://doi.org/10.1046/j.1365-246X.2003.01822.x.

Holbrook, W.S., Hoskins, H., Wood, W.T., Stephen, R.A., Lizarralde, D., 1996. Methane hydrate and free gas on the Blake Ridge from vertical seismic profiling. Science 273 (5283), 1840–1843. https://doi.org/10.1126/science.273.5283.1840.

Holland, M., Schultheiss, P., Roberts, J., Druce, M., 2008. Observed gas hydrate morphologies in marine sediments. In: 6th International Conference on Gas Hydrates. BC, Canada, Chevron, Vancouver, pp. 6–10.

Hovland, M., Gallagher, J.W., Clennell, M.B., Lekvam, K., 1997. Gas hydrate and free gas volumes in marine sediments: example from the Niger Delta front. Mar. Petrol. Geol. 14 (3), 245–255.

Hyndman, R.D., Spence, G.D., 1992. A seismic study of methane hydrate marine bottom simulating reflectors. *J. Geophy. Res.: Solid Earth* 97 (B5), 6683–6698. https://doi.org/10.1029/92JB00234.

Jakobsen, M., Hudson, J.A., Minshull, T.A., Singh, S.C., 1997. Elastic properties of hydrate-bearing sediments using effective medium theory. *J. Geophy. Res.: Solid Earth* 105 (B1), 561–577. https://doi.org/10.1029/1999JB900190.

Japsen, P., Mukerji, T., Mavko, G., 2007. Constraints on velocity-depth trends from rock physics models. Geophys. Prospect. 55, 135–154.

Kars, M., Greve, A., Zerbst, L., 2021. Authigenic greigite as an indicator of methane diffusion in gas hydrate-bearing sediments of the Hikurangi Margin, New Zealand. Front. Earth Sci. 9, 603363 https://doi.org/10.3389/feart.2021.603363.

Ker, S., Thomas, Y., Riboulot, V., et al., 2019. Anomalously deep BSR related to a transient state of the gas hydrate system in the western Black Sea. G-cubed 20, 442–459. https://doi.org/10.1029/2018GC007861.

Klaucke, I., Sahling, H., Weinrebe, W., Blinova, V., Bürk, D., Lursmanashvili, N., Bohrmann, G., 2006. Acoustic investigation of cold seeps offshore Georgia, eastern Black Sea. Mar. Geol. 231 (1–4), 51–67. https://doi.org/10.1016/j.margeo.2006.05.011.

Korenaga, J., Holbrook, W.S., Kent, G.M., Kelemen, P.B., Detrick, R.S., Larsen, H.C., et al., 2000. Crustal structure of the southeast Greenland margin from joint refraction and reflection seismic tomography. J. Geophys. Res. Solid Earth 105 (B9), 21591–21614. https://doi.org/10.1029/2000JB900188.

Kruglyakova, R.P., Byakov, Y.A., Kruglyakova, M.V., Chalenko, L.A., Shevtsova, N.T., 2004. Natural oil and gas seeps on the Black Sea floor. Geo Mar. Lett. 24 (3), 150–162.

Kunath, P., Chi, W.C., Berndt, C., Chen, L., Liu, C.S., Kläschen, D., Muff, S., 2020. A shallow seabed dynamic gas hydrate system off SW Taiwan: results from 3-D seismic, thermal, and fluid migration analyses. J. Geophys. Res. Solid Earth 125 (11) e2019JB019245-T.

Kvenvolden, K.A., 1993. Gas hydrates—geological perspective and global change. Rev. Geophys. 31 (2), 173–187. https://doi.org/10.1029/93RG00268.

Kvenvolden, K.A., 2000. Natural gas hydrate: background and history of discovery. In: Natural Gas Hydrate. Springer, Dordrecht, pp. 9–16.

De La Fuente, M., Vaunat, J., Marín-Moreno, H., 2021. Modelling methane hydrate saturation in pores: capillary inhibition effects. Energies 14 (18), 5627. https://doi.org/10.3390/en14185627.

Liao, J., Liu, X., Zhao, Q., Gong, J., Yin, W., Li, S., et al., 2022. Characteristics of high saturation hydrate reservoirs in the low-angle subduction area of the makran accretionary prism. Front. Earth Sci. 10, 861162 https://doi.org/10.3389/feart.2022.861162.

Limonov, A.F., Van Weering, T.C., Kenyon, N.H., Ivanov, M.K., Meisner, L.B., 1997. Seabed morphology and gas venting in the Black Sea mudvolcano area: observations with the MAK-1 deep-tow sidescan sonar and bottom profiler. Mar. Geol. 137 (1–2), 121–136.

Lin, A.T., Liu, C.S., Lin, C.C., Schnurle, P., Chen, G.Y., Liao, W.Z., et al., 2008. Tectonic features associated with the overriding of an accretionary wedge on top of a rifted continental margin: an example from Taiwan. Mar. Geol. 255 (3–4), 186–203.

Liu, X., Flemings, P.B., 2006. Passing gas through the hydrate stability zone at southern Hydrate Ridge, offshore Oregon. Earth Planet Sci. Lett. 241 (1–2), 211–226. https://doi.org/10.1016/j.epsl.2005.10.026.

Liu, B., Syed, W.H., Chen, J., Deng, X., Yang, L., Azevedo, L., Duan, M., Wu, T., Li, K., 2021. Distinct BSRs and their implications for natural gas hydrate formation and distribution at the submarine Makran accretionary zone. J. Oceanol. Limnol. 39 (5), 1871–1886. https://doi.org/10.1007/s00343-021-0293-9.

Lüdmann, T., Wong, H.K., Konerding, P., Zillmer, M., Petersen, J., Flüh, E., 2004. Heat flow and quantity of methane deduced from a gas hydrate field in the vicinity of the Dnieper Canyon, northwestern Black Sea. Geo-Marine Letters 24, 182–193. https://doi.org/10.1007/s00367-004-0169-y.

MacKay, M.E., Jarrard, R.D., Westbrook, G.K., Hyndman, R.D., 1994. Origin of bottom-simulating reflectors: geophysical evidence from the Cascadia accretionary prism. Geology 22 (5), 459–462.

Malinverno, A., 2010. Marine gas hydrates in thin sand layers that soak up microbial methane. Earth Planet Sci. Lett. 292, 399–408. https://doi.org/10.1016/j.epsl.2010.02.008.

Manheim, F.T., Schug, D.M., 1978. INTERSTITIAL WATERS OF BLACK SEA CORES.

Marín-Moreno, H., Giustiniani, M., Tinivella, U., Piñero, E., 2016. The challenges of quantifying the carbon stored in Arctic marine gas hydrate. Mar. Petrol. Geol. 71, 76–82. https://doi.org/10.1016/j.marpetgeo.2015.11.014.

Marín-Moreno, H., Sahoo, S.K., Best, A.I., 2017. Theoretical modeling insights into elastic wave attenuation mechanisms in marine sediments with pore-filling methane hydrate. J. Geophys. Res. Solid Earth 122, 1835–1847. https://doi.org/10.1002/2016JB013577.

Marín-Moreno, H., Giustiniani, M., Tinivella, U., 2015. The potential response of the hydrate reservoir in the South Shetland Margin, Antarctic Peninsula, to ocean warming over the 21st century. Polar Res. 34 (1), 27443 https://doi.org/10.3402/polar.v34.27443.

Mavko, G., Mukerji, T., Dvorkin, J., 2009. The Rock Physics Handbook, second ed. Cambridge Univ. Press, New York.

Mazzini, A., Ivanov, M.K., Parnell, J., Stadnitskaia, A., Cronin, B.T., Poludetkina, E., et al., 2004. Methane-related authigenic carbonates from the Black Sea: geochemical characterisation and relation to seeping fluids. Mar. Geol. 212 (1–4), 153–181.

Meisner, A., Krylov, O., Nemčok, M., 2009. Development and structural architecture of the eastern Black Sea. Lead. Edge 28 (9), 1046–1055.

Menlikli, C., Demirer, A., Sipahioglu, O., Korpe, L., Aydemir, V., 2009. Exploration plays in the Turkish Black Sea. Lead. Edge 28 (9), 1066–1075. https://doi.org/10.1190/1.3236376.

Merey, Ş, 2017. Analysis of the Black Sea gas hydrates [Thesis]. http://etd.lib.metu.edu.tr/upload/12620882/index.pdf.

Merey, S., Sinayuc, C., 2016. Investigation of gas hydrate potential of the Black Sea and modelling of gas production from a hypothetical Class 1 methane hydrate reservoir in the Black Sea conditions. J. Nat. Gas Sci. Eng. 29, 66–79.

Michaelis, W., Seifert, R., Nauhaus, K., Treude, T., Thiel, V., Blumenberg, M., et al., 2002. Microbial reefs in the Black Sea fueled by anaerobic oxidation of methane. Science 297 (5583), 1013–1015. https://doi.org/10.1126/science.1072502.

Milanovsky, E.E., 1991. Geology of the USSR 3.

Millero, F.J., Chen, C.-T., Bradshaw, A., Schleicher, K., 1980. A new high pressure equation of state for seawater. Deep-Sea Res., Part A 27 (3), 255–264. https://doi.org/10.1016/0198-0149(80)90016-3.

Minshull, T.A., Keddie, A., 2010. Measuring the geotherm with gas hydrate bottom-simulating reflectors: a novel approach using three-dimensional seismic data from the eastern Black Sea. Terra. Nova 22 (2), 131–136.

Monteleone, V., Minshull, T.A., Marin-Moreno, H., 2019. Spatial and temporal evolution of rifting and continental breakup in the Eastern Black Sea Basin revealed by long-offset seismic reflection data. Tectonics 38 (8), 2646–2667. https://doi.org/10.1029/2019TC005523.

Moridis, G.J., 2003. Numerical studies of gas production from methane hydrates. Soc. Pet. Eng. J. 32 (8), 359–370. https://doi.org/10.2118/75691-MS.

Mosher, D.C., 2011. A margin-wide BSR gas hydrate assessment: Canada's Atlantic margin. Marine and Petroleum Geology 28 (8), 1540–1553. https://doi.org/10.1016/j.marpetgeo.2011.06.007.

Muratov, M.V., Neprochnov, Y.P., Ross, D.A., Trimonis, E.S., 1978. Basic Features of the Black Sea Late Cenozoic History Based on the Results of Deep-Sea Drilling leg 42B1.

Nasif, A., Özel, F.E., Dondurur, D., 2020. Seismic identification of gas hydrates: a case study from Sakarya Canyon, western Black Sea. Turk. J. Earth Sci. 29 (3), 434–454. https://doi.org/10.3906/yer-1909-2.

Nikishin, A.M., Korotaev, M.V., Ershov, A.V., Brunet, M.F., 2003. The Black Sea basin: tectonic history and Neogene–Quaternary rapid subsidence modelling. Sediment. Geol. 156, 149–168.

Nole, M., Daigle, H., Cook, A.E., Malinverno, A., 2016. Short-range, overpressure-driven methane migration in coarse-grained gas hydrate reservoirs. Geophys. Res. Lett. 43, 9500–9508. https://doi.org/10.1002/2016GL070096.

Okay, A.I., Celal Sengor, A.M., Gorur, N., 1994. Kinematic history of the opening of the Black Sea and its effect on the surrounding regions. Geology 22 (3), 267–270.

Østergaard, K.K., Anderson, R., Llamedo, M., Tohidi, B., 2002. Hydrate phase equilibria in porous media: effect of pore size and salinity. Terra. Nova 14 (5), 307–312. https://doi.org/10.1046/j.1365-3121.2002.00433.x.

Özsoy, E., Ünlüata, Ü., 1997. Oceanography of the Black Sea: a review of some recent results. Earth Sci. Rev. 42 (4), 231–272.

Pape, T., Bahr, A., Klapp, S.A., Abegg, F., Bohrmann, G., 2011. High-intensity gas seepage causes rafting of shallow gas hydrates in the southeastern Black Sea. Earth Planet Sci. Lett. 307 (1–2), 35–46.

Pape, T., Blumenberg, M., Reitz, A., Scheeder, G., Schmidt, M., Haeckel, M., et al., 2021. Oil and gas seepage offshore Georgia (Black Sea)–Geochemical evidences for a Paleogene-Neogene hydrocarbon source rock. Mar. Petrol. Geol. 128, 104995.

Pecher, I.A., Henrys, S.A., Ellis, S., Chiswell, S.M., Kukowski, N., 2005. Erosion of the seafloor at the top of the gas hydrate stability zone on the Hikurangi Margin, New Zealand. Geophys. Res. Lett. 32 (24) https://doi.org/10.1029/2005GL024687.

Pecher, I.A., Minshull, T.A., Singh, S.C., von Huene, R., 1996. Velocity structure of a bottom simulating reflector offshore Peru: results from full waveform inversion. Earth Planet Sci. Lett. 139 (3–4), 459–469. https://doi.org/10.1016/0012-821X(95)00242-5.

Pecher, I., Villinger, H., Kaul, N., Crutchley, G.J., Mountjoy, J.J., Huhn, K., et al., 2017. A fluid pulse on the Hikurangi subduction margin: evidence from a heat flux transect across the upper limit of gas hydrate stability. Geophys. Res. Lett. 44 (24), 12–385.

Poort, J., Vassilev, A., Dimitrov, L., 2005. Did postglacial catastrophic flooding trigger massive changes in the Black Sea gas hydrate reservoir? Terra. Nova 17 (2), 135–140.

Popescu, I., De Batist, M., Lericolais, G., Nouzé, H., Poort, J., Panin, N., et al., 2006. Multiple bottom-simulating reflections in the Black Sea: potential proxies of past climate conditions. Marine *Geology*, 227 (3–4), 163–176.

Popescu, I., Lericolais, G., Panin, N., De Batist, M., Gillet, H., 2007. Seismic expression of gas and gas hydrates across the western Black Sea. Geo Mar. Lett. 27 (2–4), 173–183.

Portnov, A., Cook, A.E., Sawyer, D.E., 2022. Bottom simulating reflections and seismic phase reversals in the Gulf of Mexico. World Atlas of Submarine Gas Hydrates in Continental Margins 315–322. ISBN : 978-3-030-81185-3.

Portnov, A., Cook, A.E., Vadakkepuliyambatta, S., 2021. Diverse gas composition controls the Moby-Dick gas hydrate system in the Gulf of Mexico. Geology 49 (12), 1446–1451. https://doi.org/10.1130/G49310.1.

Posewang, J., Mienert, J., 1999. The enigma of double BSRs: indicators for changes in the hydrate stability field? Geo Mar. Lett. 19 (1–2), 157–163.

Priest, J.A., Best, A.I., Clayton, C.R.I., 2009. Influence of gas hydrate morphology on the seismic velocities of sands, 114. https://doi.org/10.1029/2009JB006284.

Qin, Y., Singh, S.C., 2018. Insight into frontal seismogenic zone in the Mentawai locked region from seismic full waveform inversion of ultralong offset streamer data. G-cubed 19 (11), 4342–4365. https://doi.org/10.1029/2018GC007787.

Reed, D.L., Silver, E.A., Tagudin, J.E., Shipley, T.H., Vrolijk, P., 1990. Relations between mud volcanoes, thrust deformation, slope sedimentation, and gas hydrate, offshore north Panama. Mar. Petrol. Geol. 7 (1), 44–54.

Reilinger, R., McClusky, S., Vernant, P., Lawrence, S., Ergintav, S., Cakmak, R., Ozener, H., Kadirov, F., Guliev, I., Stepanyan, R., Nadariya, M., Hahubia, G., et al., 2006. GPS constraints on continental deformation in the Africa– Arabia–Eurasia continental collision zone and implications for the dynamics of plate interactions. J. Geophys. Res. 111 https://doi.org/10.1029/2005JB004051.

Ren, X., Guo, Z., Ning, F., Ma, S., 2020. Permeability of hydrate-bearing sediments. Earth Sci. Rev. 202, 103100 https://doi.org/10.1016/j.earscirev.2020.103100.

Riboulot, V., Ker, S., Sultan, N., Thomas, Y., Marsset, B., Scalabrin, C., et al., 2018. Freshwater lake to salt-water sea causing widespread hydrate dissociation in the Black Sea. Nat. Commun. 9 (1), 1–8.

Riedel, M., Bialas, J., Villinger, H., Pape, T., Haeckel, M., Bohrmann, G., 2021. Heat flow measurements at the danube deep-sea Fan,Western Black Sea. Geosciences 11, 240. https://doi.org/10.3390/geosciences11060240.

Riedel, M., Collett, T.S., 2017. Observed correlation between the depth to base and top of gas hydrate occurrence from review of global drilling data. Geochemistry, Geophysics, Geosystems 18 (7), 2543–2561. https://doi.org/10.1002/2017GC006805.

Riedel, M., Freudenthal, T., Bergenthal, M., Haeckel, M., Wallmann, K., Spangenberg, E., et al., 2020. Physical properties and core-log seismic integration from drilling at the Danube deep-sea fan, Black Sea. Mar. Petrol. Geol. 114, 104192.

Robinson, A.G., Kerusov, E., 1997. AAPG memoir 68: regional and petroleum geology of the Black Sea and surrounding region. In: Stratigraphic and Structural Development of the Gulf of Odessa, Ukrainian Black Sea: Implications for Petroleum Exploration (Chapter 19):

Ross, D.A., 1978. Summary of results of Black Sea drilling. Init. Rep. DSDP 42, 1149–1177.

Ross, D.A., Neprchnov, Y.P., Hsu, K.J., Trimonis, E.S., Percival Jr., S.F., Erickson, A.J., Degens, E.T., Hunt, J.M., Manheim, F.T., Senalp, M., Traverse, A., Stoffers, P., 1978. Leg 42, Part 2, of the Cruises of the Drilling Vessel Glomar Challenger; Istanbul, Turkey to Istanbul, Turkey, May–June 1975. DSDP.

Ruppel, C.D., Kessler, J.D., 2017. The interaction of climate change and methane hydrates. Rev. Geophys. 55 (1), 126–168.

Ryan, W.B., Major, C.O., Lericolais, G., Goldstein, S.L., 2003. Catastrophic flooding of the Black Sea. Annual Review of Earth and Planetary Sciences 31 (1), 525–554. https://doi.org/10.1146/annurev.earth.31.100901.141249.

Sahling, H., Bohrmann, G., Artemov, Y.G., Bahr, A., Brüning, M., Klapp, S.A., et al., 2009. Vodyanitskii mud volcano, Sorokin trough, Black Sea: geological characterization and quantification of gas bubble streams. Mar. Petrol. Geol. 26 (9), 1799–1811. https://doi.org/10.1016/j.marpetgeo.2009.01.010.

Sahoo, S.K., Marín-Moreno, H., North, L.J., Falcon-Suarez, I., Madhusudhan, B.N., Best, A.I., Minshull, T.A., 2018. Presence and consequences of coexisting methane gas with hydrate under two phase water-hydrate stability conditions. J. Geophys. Res. Solid Earth 123 (5), 3377–3390. https://doi.org/10.1029/2018JB015598.

Sahoo, S.K., North, L.J., Marín-Moreno, H., Minshull, T.A., Best, A.I., 2019. Laboratory observations of frequency-dependent ultrasonic P-wave velocity and attenuation during methane hydrate formation in Berea sandstone. Geophys. J. Int. 219 (1), 713–723. https://doi.org/10.1093/gji/ggz311.

Saintot, A., Brunet, M.F., Yakovlev, F., Sébrier, M., Stephenson, R., Ershov, A., et al., 2006. The mesozoic-cenozoic tectonic evolution of the greater Caucasus. Geological Society, London, Memoirs 32 (1), 277–289.

Schneider, F., Dubille, M., Montadert, L., 2016. Modeling of microbial gas generation: application to the eastern mediterranean "biogenic play". Geol. Acta 14, 403–417. https://doi.org/10.1344/GeologicaActa2016.1314.1344.1345.

Scott, C.L., Shillington, D.J., Minshull, T.A., Edwards, R.A., Brown, P.J., White, N.J., 2009. Wide-angle seismic data reveal extensive overpressures in the Eastern Black Sea Basin. Geophys. J. Int. 178 (2), 1145–1163.

Screaton, E.J., Torres, M.E., Dugan, B., Heeschen, K.U., Mountjoy, J.J., Ayres, C., Rose, P.S., Pecher, I.A., Barnes, P.M., 2019. Sedimentation controls on methane-hydrate dynamics across glacial/interglacial stages: An example from International Ocean Discovery Program Site U1517, Hikurangi Margin. Geochemistry, Geophysics, Geosystems 20 (11), 4906–4921. https://doi.org/10.1029/2019GC008603.

Setzmann, U., Wagner, W., 1991. A new equation of state and tables of thermodynamic properties for methane covering the range from the melting line to 625 K at pressures up to 100 MPa. J. Phys. Chem. Ref. Data 20 (6), 1061–1155. https://doi.org/10.1063/1.555898.

Sheremet, Y., Sosson, M., Ratzov, G., Sydorenko, G., Voitsitskiy, Z., Yegorova, T., et al., 2016. An offshore-onland transect across the north-eastern Black Sea basin (Crimean margin): evidence of Paleocene to Pliocene two-stage compression. Tectonophysics 688, 84–100.

Shillington, D.J., White, N., Minshull, T.A., Edwards, G.R., Jones, S.M., Edwards, R.A., Scott, C.L., 2008. Cenozoic evolution of the eastern Black Sea: a test of depth-dependent stretching models. Earth Planet Sci. Lett. 265 (3–4), 360–378.

Shipley, T.H., Houston, M.H., Buffler, R.T., Shaub, F.J., McMillen, K.J., Laod, J.W., Worzel, J.L., 1979. Seismic evidence for widespread possible gas hydrate horizons on continental slopes and rises. AAPG Bull. 63 (12), 2204–2213. https://doi.org/10.1306/2F91890A-16CE-11D7-8645000102C1865D.

Shnyukov, E.F., 2013. Mud volcanoes of the Black Sea as a prospecting indicator of methane gas hydrates. Lithol. Miner. Resour. 48 (2), 114.

Simmons, M.D., Tari, G.C., Okay, A.I., 2018. Petroleum geology of the Black Sea: introduction. Geological Society, London, Special Publications 464 (1), 1–18.

Singh, S.C., Minshull, T.A., Spence, G.D., 1993. Velocity structure of a gas hydrate reflector. Science 260 (5105), 204–207. https://doi.org/10.1126/science.260.5105.204.

Sloan, E.D., 1998. Gas hydrates: review of physical/chemical properties. Energy Fuel. 12 (2), 191–196.

Soulet, G., Delaygue, G., Vallet-Coulomb, C., et al., 2010. Glacial hydrologic conditions in the Black Sea reconstructed using geochemical pore water profiles. Earth Planet Sci. Lett. 296, 57–66. https://doi.org/10.1016/j.epsl.2010.04.045.

Spangenberg, E., Priegnitz, M., Heeschen, K., Schicks, J.M., 2014. Are laboratory-formed hydrate-bearing systems analogous to those in nature? J. Chem. Eng. Data 60, 258–268. https://doi.org/10.1021/je5005609.

Starostenko, V.I., Rusakov, O.M., Shnyukov, E.F., Kobolev, V.P., Kutas, R.I., 2010. Methane in the northern Black Sea: characterization of its geomorphological and geological environments. Geological Society, London, Special Publications 340 (1), 57–75.

Stephenson, R., Schellart, W.P., 2010. The Black Sea back-arc basin: insights to its origin from geodynamic models of modern analogues. Geological Society, London, Special Publications 340 (1), 11–21.

Stoll, R.D., Bryan, G.M., 1970. Wave attenuation in saturated sediments. J. Acoust. Soc. Am. 47 (5B), 1440–1447. https://doi.org/10.1121/1.1912054.

Taladay, K., Boston, B., Moore, G.F., 2017. Gas-in-place estimate for potential gas hydrate concentrated zone in the Kumano Basin, Nankai Trough Forearc, Japan. Energies 10 (10), 1552.

Tari, G.C., Simmons, M.D., 2018. History of deepwater exploration in the Black Sea and an overview of deepwater petroleum play types. Geological Society, London, Special Publications 464 (1), 439–475.

Tari, G., Vakhania, D., Tatishvili, G., Mikeladze, V., Gogritchiani, K., Vacharadze, S., et al., 2018. Stratigraphy, structure and petroleum exploration play types of the Rioni Basin, Georgia. Geological Society, London, Special Publications 464 (1), 403–438.

Tinivella, U., Giustiniani, M., 2013. Variations in BSR depth due to gas hydrate stability versus pore pressure. Global Planet. Change 100, 119–128. https://doi.org/10.1016/j.gloplacha.2012.10.012.

Tugolesov, D.A., Gorshkov, A.S., 1985. Tectonics of the Mesozoic Sediments of the Black Sea Basin. Nedra, Moscow ([in Russian]).

Vassilev, A., Dimitrov, L., 2002. Spatial and quantity evaluation of the Black Sea gas hydrates. Russ. Geol. Geophys. 43 (7), 672–684.

Vassilev, A., 2006. Black Sea gas hydrates stability zone model (Optimistic & Pessimistic Assessment). In: CRIMEA Final Project Meeting, January 19-21, 2006 (Gent, Belgium).

Vincent, S.J., Morton, A.C., Carter, A., Gibbs, S., Barabadze, T.G., 2007. Oligocene uplift of the western greater Caucasus: an effect of initial arabia–eurasia collision. Terra. Nova 19 (2), 160–166.

Wang, X., Collett, T.S., Lee, M.W., Yang, S., Guo, Y., Wu, S., 2014. Geological controls on the occurrence of gas hydrate from core, downhole log, and seismic data in the Shenhu area, South China Sea. Mar. Geol. 357, 272–292. https://doi.org/10.1016/j.margeo.2014.09.040.

Wang, J., Wu, S., Kong, X., Li, Q., Wang, J., Ding, R., 2018. Geophysical characterization of a fine-grained gas hydrate reservoir in the Shenhu area, northern South China Sea: integration of seismic data and downhole logs. Mar. Petrol. Geol. 92, 895–903. https://doi.org/10.1016/j.marpetgeo.2018.03.020.

Waite, W.F., Santamarina, J.C., Cortes, D.D., Dugan, B., Espinoza, D.N., Germaine, J., et al., 2009. Physical properties of hydrate-bearing sediments. Rev. Geophys. 47 (4).

Waite, W.F., Jang, J., Collett, T.S., Kumar, P., 2019. Downhole physical property-based description of a gas hydrate petroleum system in NGHP-02 Area C: a channel, levee, fan complex in the Krishna-Godavari Basin offshore eastern India. Mar. Petrol. Geol. 108, 272–295. https://doi.org/10.1016/j.marpetgeo.2018.05.021.

Wood, W.T., Ruppel, C., 2000. Seismic and thermal investigations of the Blake Ridge gas hydrate area: a synthesis. Proceedings of the Ocean Drilling Program. Scientific results. Ocean Drilling Program 253–264.

Woodside, J.M., Modin, D.I., Ivanov, M.K., 2003. An enigmatic strong reflector on subbottom profiler records from the Black Sea—the top of shallow gas hydrate deposits. Geo Mar. Lett. 23, 269–277. https://doi.org/10.1007/s00367-003-0149-7.

Xing, J., Spiess, V., 2015. Shallow gas transport and reservoirs in the vicinity of deeply rooted mud volcanoes in the central Black Sea. Mar. Geol. 369, 67–78.

You, K., Flemings, P.B., 2018. Methane hydrate formation in thick sandstones by free gas flow. J. Geophys. Res. Solid Earth 123, 4582–4600. https://doi.org/10.1029/2018JB015683.

You, K., Flemings, P.B., Malinverno, A., Collett, T.S., Darnell, K., 2019. Mechanisms of methane hydrate formation in geological systems. Rev. Geophys. 57 (4), 1146–1196. https://doi.org/10.1029/2018RG000638.

Zander, T., Haeckel, M., Berndt, C., Chi, W.C., Klaucke, I., Bialas, J., et al., 2017. On the origin of multiple BSRs in the Danube deep-sea fan, Black Sea. Earth Planet Sci. Lett. 462, 15–25. https://doi.org/10.1016/j.epsl.2017.01.006.

Zander, T., Haeckel, M., Klaucke, I., Bialas, J., Klaeschen, D., Papenberg, C., et al., 2020. New insights into geology and geochemistry of the Kerch seep area in the Black Sea. Mar. Petrol. Geol. 113, 104162 https://doi.org/10.1016/j.marpetgeo.2019.104162.

Zelt, C.A., Smith, R.B., 1992. Seismic traveltime inversion for 2-D crustal velocity structure. Geophys. J. Int. 108 (1), 16–34.

Zillmer, M., Flueh, E.R., Petersen, J., 2005. Seismic investigation of a bottom simulating reflector and quantification of gas hydrate in the Black Sea. Geophys. J. Int. 161 (3), 662–678.